

# Spontaneous symmetry breaking in graphene subjected to an in-plane magnetic field

I. L. Aleiner,<sup>1</sup> D. E. Kharzeev,<sup>2</sup> and A. M. Tsvelik<sup>3,4</sup>

<sup>1</sup>Physics Department, Columbia University, New York, New York 10027, USA

<sup>2</sup>Department of Physics, Brookhaven National Laboratory, Upton, New York 11973-5000, USA

<sup>3</sup>Department of Condensed Matter Physics and Materials Science, Brookhaven National Laboratory, Upton, New York 11973-5000, USA

<sup>4</sup>Department of Physics and Astronomy, SUNY at Stony Brook, Stony Brook, New York 11794-3800, USA

(Received 2 August 2007; published 14 November 2007)

Application of the magnetic field parallel to the plane of the graphene sheet leads to the formation of electron- and holelike Fermi surfaces. Such situation is shown to be unstable with respect to the formation of an excitonic condensate even for an arbitrary weak magnetic field and interaction strength. At temperatures lower than the mean-field temperature, the order parameter amplitude is formed. The order parameter itself is a U(2) matrix allowing for the combined rotations in the spin and valley spaces. These rotations smoothly interpolate between site and bond centered spin-density waves and spin-flux states. The trigonal warping, short-range interactions, and the three-particle umklapp processes freeze some degrees of freedom at temperatures much smaller than the mean-field transition temperature, and make either Berezinskii-Kosterlitz-Thouless [Sov. Phys. JETP **32**, 493 (1971); J. Phys. C **5**, L124 (1972); **6**, 1181 (1973)] (driven either by vortices or half-vortices) or Ising type transitions possible. Strong logarithmic renormalization for the coupling constants of these terms by the Coulomb interaction is calculated within one-loop renormalization group. It is found that in the presence of the Coulomb interaction, some short-range interaction terms become much greater than one might expect from the naive dimensionality counting.

DOI: 10.1103/PhysRevB.76.195415

PACS number(s): 73.63.-b, 81.05.Uw, 72.15.Rn

## I. INTRODUCTION

The fabrication of graphene (graphite monolayers<sup>1,2</sup>) and the subsequent observation of the integer quantum Hall<sup>3,4</sup> in this layer produced a splash of theoretical and experimental activity.

Though the transport properties of graphene are controlled by the impurities, it is still worthwhile to understand the phase diagram of the completely clean graphene.

The main purpose of this paper is to point out that an application of a magnetic field in the graphene plane facilitates a spontaneous symmetry breaking. Though the dimensionless Coulomb coupling  $e^2/\hbar v$  in graphene is large at large energies, it undergoes strong downward renormalization at small energies so that the analysis for weak magnetic fields can be safely carried out without resorting to any uncontrollable approximations.<sup>5</sup>

To achieve this goal and understand the effects of the naively dimensionally irrelevant terms (such as trigonal warping, short-range part of the interaction, and umklapp terms), we considered their logarithmic renormalization by the long-range Coulomb interaction and found some unexpected results. Earlier, the effect of the Coulomb interaction was considered for the isotropic terms only.<sup>6-8</sup>

The remainder of the paper is organized as follows. In Sec. II, we discuss symmetries of a two-dimensional graphene sheet and write down its low-energy Hamiltonian. In Sec. III, we describe physical reasons for the instability and suggest the order parameter. In Sec. IV, we write down the Landau-Ginzburg free energy functional, discuss thermal fluctuations, and describe the phase diagram. Section V is devoted to the analysis of the microscopics: we study the energy dependence of the effective coupling and renormalization of the leading anisotropies in graphene. Section VI

contains the summary and conclusions. Some auxiliary materials are relegated into two appendixes.

## II. SYMMETRIES OF THE SYSTEM AND THE MODEL LOW-ENERGY HAMILTONIAN

The purpose of this section is to write down the low-energy field theory to describe the electron-electron interaction in graphene. Our consideration will be based on the discrete symmetries of the lattice only, and we will not appeal to any microscopic model.<sup>9</sup>

The effective low-energy field theory of graphene is constructed by the factorization of the original fermionic fields  $\Psi_\sigma(\mathbf{r}; \tau)$ ,  $\sigma = \uparrow, \downarrow$ , in terms of the oscillatory Bloch functions corresponding to the  $K$  and  $K'$  points of the Brillouin zone (see Fig. 1),

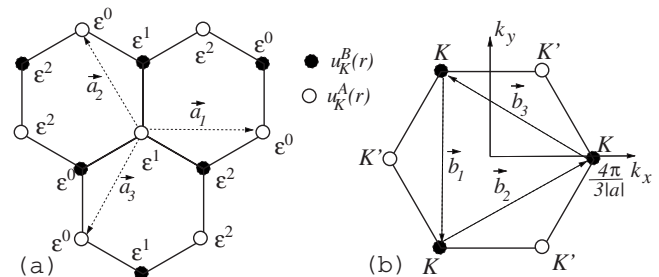


FIG. 1. (a) The hexagonal lattice of graphene with the shortest translation vectors  $\vec{a}_{1,2,3}$ . Circles show the positions of the maxima of the absolute values of Bloch functions  $u_K^{A,B}(\mathbf{r})$ . Their relative phases are shown,  $\epsilon = \exp(i2\pi/3)$ . (b) The first Brillouin zone and the shortest translation vectors of the reciprocal lattice  $\vec{b}_{1,2,3}$ . Two nonequivalent Dirac cones are formed in the vicinity of points  $K$  and  $K'$ .

$$\Psi_{\sigma}(\mathbf{r}; \tau) = \vec{\psi}_{\sigma}(\mathbf{r}, \tau)^* \vec{u}(\mathbf{r}), \quad (2.1)$$

where  $\psi_{\sigma}(\mathbf{r}, \tau)$  is the four component fermionic field which can vary only over distances much larger than the lattice constant, and  $\vec{u}(\mathbf{r})$  is the four-dimensional vector of the Bloch functions whose structure is described below.

Consider the Bloch functions ( $u^A(\mathbf{r})_K, u^B(\mathbf{r})_K$ ) forming a basis for a two-dimensional irreducible representation of the wave-vector symmetry group  $C_{3v}$ . (In the tight-binding picture, those Bloch functions are peaked on the corresponding sublattices; see Fig. 1). The overall point symmetry group is  $C_{6v}$ , and thus, the wave functions  $u^A_K = [u^A_K]^*$  and  $u^B_{K'} = [u^B_{K'}]^*$  also have to be included as points  $K'$  and  $K$  are connected to each other by  $C_2$  rotation and by time reversal symmetry. They are conveniently joined in a vector<sup>10</sup>

$$\vec{u}^T = ((u^A_K; u^B_K)_{AB} (u^B_{K'}; -u^A_{K'})_{AB})_{KK'}, \quad (2.2)$$

forming the basis of the four-dimensional irreducible representation of the planar symmetry group of graphene  $\sum_{j_1, j_2} C_{6v}^{j_1} \tilde{a}_1 + j_2 \tilde{a}_2$ , with the normalization condition

$$\int_{uc} d\mathbf{r} \vec{u}(\mathbf{r}) \cdot \vec{u}^*(\mathbf{r}) = 4|\tilde{a}_1 \times \tilde{a}_2|. \quad (2.3)$$

Hereinafter,  $\int_{uc}$  denotes integration within the unit cell.

Thus, the fermionic field describing all relevant degrees of freedom,  $\boldsymbol{\psi}^T = (\psi_{\uparrow}, \psi_{\downarrow})$ , has eight components. This eight-dimensional space is represented [see Eq. (2.2)] as a direct product of the valley ( $KK'$ ), the sublattice ( $AB$ ), and the spin ( $s$ ) two-dimensional spaces. We will use standard  $2 \times 2$  Pauli matrices  $\hat{\tau}_{x,y,z}$ , with the corresponding subscripts to parametrize all  $8 \times 8$  matrices describing the Hamiltonian and the symmetry properties.

The partition function describing the low-energy properties of the interacting electrons in a clean graphene is given by ( $\hbar=1$ )

$$\mathcal{Z} = \int \mathcal{D}\boldsymbol{\psi}^{\dagger} \mathcal{D}\boldsymbol{\psi} \exp \left\{ - \int_0^{1/T} d\tau \int d\mathbf{r} \left[ \boldsymbol{\psi}^{\dagger} \frac{\partial \boldsymbol{\psi}}{\partial \tau} + H(\boldsymbol{\psi}^{\dagger}, \boldsymbol{\psi}) \right] \right\}. \quad (2.4)$$

The Hamiltonian of the system has to satisfy all the discrete symmetries of the clean graphene, and to remain invariant with respect to transformations of the fields generated by the rotation  $C_3$ , two reflections  $\sigma_v^{x,y}$ , and translations ( $t$ ):

$$C_3: \boldsymbol{\psi}(\mathbf{r}) \rightarrow - \exp \left[ \theta^C \left( \mathbf{r} \times \nabla + \frac{i}{2} \hat{\Sigma}_z \right) \right] \boldsymbol{\psi}(\mathbf{r}), \quad (2.5a)$$

$$\sigma_v^x: \boldsymbol{\psi}(x, y) \rightarrow \hat{\Sigma}_x \hat{\Lambda}_z \boldsymbol{\psi}(x, -y), \quad (2.5b)$$

$$\sigma_v^y: \boldsymbol{\psi}(x, y) \rightarrow \hat{\Sigma}_y \hat{\Lambda}_x \boldsymbol{\psi}(-x, y), \quad (2.5c)$$

$$t: \boldsymbol{\psi}(\mathbf{r}) \rightarrow \exp[i\theta^t \hat{\Lambda}_z] \boldsymbol{\psi}(\mathbf{r}), \quad (2.5d)$$

where  $\theta^{C,t} = \pm 2\pi/3$ , and we introduce the matrices

$$\hat{\Sigma}_{\alpha} = \hat{\tau}_{\alpha}^{AB} \otimes \mathbb{1}^{KK'} \otimes \mathbb{1}^s,$$

$$\hat{\Lambda}_{\alpha} = \mathbb{1}^{AB} \otimes \hat{\tau}_{\alpha}^{KK'} \otimes \mathbb{1}^s,$$

$$\hat{S}_{\alpha} = \mathbb{1}^{AB} \otimes \mathbb{1}^{KK'} \otimes \hat{\tau}_{\alpha}^s, \quad (2.6)$$

where  $\alpha=x, y$ , and  $z$ .

Continuous  $U(1)$  rotations in the spin space are given by

$$U(1): \boldsymbol{\psi} \rightarrow \exp(i\theta_s \hat{S}_z/2) \boldsymbol{\psi}, \quad (2.7)$$

where we choose the  $z$  direction of the spin to be along the magnetic field.

Time reversal symmetry for the parametrization (2.2) acquires a natural form

$$\mathcal{T}: \boldsymbol{\psi}(\tau) \rightarrow \hat{\tau}_y^{AB} \otimes \hat{\tau}_y^{KK'} \otimes \hat{\tau}_y^s \boldsymbol{\psi}^*(-\tau), \quad \mathcal{B} \rightarrow -\mathcal{B}, \quad (2.8)$$

where  $\mathcal{B}$  is the magnetic field acting, in our case, only on the electron spin.

Having listed the important symmetries of the problem, we present the Hamiltonian in the form

$$H = H_D + H_C + H_w + H_{sr} + H_u. \quad (2.9)$$

The first term describes the Dirac-type kinetic energy and the Zeeman energy

$$H_D = -iv(r_c) \boldsymbol{\psi}^{\dagger} \nabla \cdot \hat{\Sigma} \boldsymbol{\psi} + \mathcal{B} \boldsymbol{\psi}^{\dagger} \hat{S}_z \boldsymbol{\psi}, \quad (2.10)$$

where  $\nabla = (\partial_x, \partial_y)$ ,  $\hat{\Sigma}$  is defined in Eq. (2.6), the Bohr magneton and the  $g$  factor are included into the definition of  $\mathcal{B}$ , and  $r_c$  is the minimal linear scale present in the problem. As was pointed out in Ref. 6 (see also Refs. 7 and 8), the velocity  $v(r_c)$  becomes scale dependent due to the Coulomb interaction

$$H_C = \frac{e^2}{2} \int d\mathbf{r}_1 \frac{[\boldsymbol{\psi}^{\dagger}(\mathbf{r}) \boldsymbol{\psi}(\mathbf{r})][\boldsymbol{\psi}^{\dagger}(\mathbf{r}_1) \boldsymbol{\psi}(\mathbf{r}_1)]}{|\mathbf{r} - \mathbf{r}_1|}, \quad (2.11)$$

whose strength  $e^2$  cannot be renormalized as it is the only nonlocal term in the system.

Though the terms described by Eqs. (2.10) and (2.11) are the most important ones on dimensional grounds, they are not sufficient to define the problem completely since their symmetries are much higher:

$$C_{\infty}: \boldsymbol{\psi}(\mathbf{r}) \rightarrow \exp \left[ \theta^C \left( \mathbf{r} \times \nabla + \frac{i}{2} \hat{\Sigma}_z \right) \right] \boldsymbol{\psi}(\mathbf{r}), \quad (2.12a)$$

$$\sigma_v: \boldsymbol{\psi}(x, y) \rightarrow \hat{\Sigma}_x \boldsymbol{\psi}(x, -y), \quad (2.12b)$$

$$U(1) \otimes SU(2) \otimes SU(2): \boldsymbol{\psi}(\mathbf{r}) \rightarrow \hat{U}(\alpha^{\pm}, \theta^s; \mathbf{n}_{1,2}) \boldsymbol{\psi}(\mathbf{r}),$$

$$\hat{U} = \exp \left[ \frac{i\alpha^{-} \mathbf{n}_2 \cdot \vec{\Lambda} \hat{S}_z}{2} \right] \exp \left[ \frac{i\theta^s \hat{S}_z}{2} \right] \exp \left[ \frac{i\alpha^{+} \mathbf{n}_1 \cdot \vec{\Lambda}}{2} \right] \quad (2.12c)$$

than it is allowed by Eqs. (2.5a), (2.5b), (2.5c), (2.5d), and

(2.6)–(2.8). Here,  $\theta$  are the continuous real variables and  $\mathbf{n}_{1,2}$  are three-dimensional unit vectors.

The terms lowering the symmetry of the Hamiltonian can appear both in the kinetic energy and in the interaction Hamiltonian. For instance, the trigonal warping of the one-electron spectrum is given by

$$H_w = \lambda_w(r_c) r_c v(r_c) \psi^\dagger [\partial_+^2 \hat{\Sigma}_+ \hat{\Lambda}_z + \text{H.c.}] \psi, \quad (2.13)$$

where  $\partial_+ \equiv \partial_x + i\partial_y$  and  $\hat{\Sigma}_+ \equiv (\hat{\Sigma}_x + i\hat{\Sigma}_y)/2$ . Dimensionless coupling  $\lambda_w(r_c)$  is of the order of unity at  $r_c$  of the order of the lattice constant, and scales down at larger distances.

In writing down the short-range interaction, one can neglect the effect of the Zeeman term on the scale of the order of the lattice constant. Thus, the SU(2) invariance in the spin space must be preserved and

$$\begin{aligned} \frac{2}{r_c v(r_c)} H_{sr} = & \sum_{\alpha, \beta=x,y,z} F_{\alpha\beta}(r_c) (\psi^\dagger \hat{\Sigma}_\alpha \hat{\Lambda}_\beta \psi)^2 \\ & + \sum_{\alpha=x,y,x} [J_\alpha^\Sigma(r_c) (\psi^\dagger \hat{\Sigma}_\alpha \psi)^2 + J_\alpha^\Lambda(r_c) (\psi^\dagger \hat{\Lambda}_\alpha \psi)^2]. \end{aligned} \quad (2.14a)$$

[All the other short-range spin rotational invariant interaction terms can be reduced to those of Eqs. (2.14a) and (2.14b) by using the identity  $2\delta_{\sigma_1\sigma_2}\delta_{\sigma_3\sigma_4} = \delta_{\sigma_1\sigma_4}\delta_{\sigma_2\sigma_3} + \hat{\tau}_{\sigma_1\sigma_4}\hat{\tau}_{\sigma_2\sigma_3}$ .]

The symmetries (2.5) immediately yield the relation

$$\begin{aligned} F_{zz} &= 2F_-^z + F_+^z, \\ F_{xz} &= F_{yz} = -F_-^z + F_+^z, \\ F_{zx} &= F_{zy} = 2F_-^\perp + F_+^\perp, \\ F_{xx} &= F_{yy} = F_{xy} = F_{yx} = -F_-^\perp + F_+^\perp, \\ J_z^{\Sigma,\Lambda} &= 2J_-^{\Sigma,\Lambda} + J_+^{\Sigma,\Lambda}, \\ J_x^{\Sigma,\Lambda} &= J_y^{\Sigma,\Lambda} = -J_-^{\Sigma,\Lambda} + J_+^{\Sigma,\Lambda}. \end{aligned} \quad (2.14b)$$

The reason for introducing  $F_\pm$  and  $J_\pm$  couplings will become clear later in Sec. V. As for the numerical values of the couplings, a very crude estimate at the scale  $r_c$  of the order of the lattice constants can be obtained by calculating the matrix elements of the bare interaction potential:

$$\begin{aligned} F_{\alpha\beta} &= \left( \frac{e^2}{4v(r_c)} \right) \int dr_1 \int_{uc} \frac{dr_2 \rho_{\alpha\beta}(\mathbf{r}_1) \rho_{\alpha\beta}(\mathbf{r}_2)}{r_c |\vec{a}_1 \times \vec{a}_2| |r_1 - r_2|}, \\ \rho_{\alpha\beta}(\mathbf{r}) &\equiv (\vec{u}(\mathbf{r}))^\dagger \hat{\Sigma}_\alpha \hat{\Lambda}_\beta \vec{u}(\mathbf{r}), \end{aligned} \quad (2.15)$$

and  $J^{\Sigma,\Lambda} = 0$ . (Obtaining finite values of  $J^{\Sigma,\Lambda}$  requires virtual processes at least of the second order.) As  $\rho_{\alpha\beta}(\mathbf{r})$  contains only oscillatory components [see Eqs. (2.2) and (2.6)], the integral in Eq. (2.15) is determined only by the distances of the order of the lattice constant. Thus, the parameters are extremely sensitive to the details at short distances and should be treated as entries for the low-energy theory.

Though the warping and the short-range interaction (2.13), (2.14a), and (2.14b) lift most of the spurious symmetries (2.12), the extra continuous U(1) symmetry is still present, corresponding to Eq. (2.5d) with continuous  $\theta^t$ . It is related to the conservation of quasimomentum, which is violated only by the umklapp processes. The lowest order term satisfying the symmetries (2.5) has the form

$$\begin{aligned} H_u = & \frac{r_c^3 v(r_c)}{6} \sum_{\alpha\beta\gamma} \mathcal{F}_{\alpha\beta\gamma}(r_c) [(\psi^\dagger \hat{\Sigma}_\alpha \hat{\Lambda}_+ \psi)(\psi^\dagger \hat{\Sigma}_\beta \hat{\Lambda}_+ \psi) \\ & \times (\psi^\dagger \hat{\Sigma}_\gamma \hat{\Lambda}_+ \psi) + \text{H.c.}], \end{aligned} \quad (2.16)$$

where  $\hat{\Lambda}_+ \equiv (\hat{\Lambda}_x + i\hat{\Lambda}_y)/2$ ,  $\mathcal{F}_{\alpha\beta\gamma}$  is symmetric with respect to permutations of the indices, and

$$\mathcal{F}_{xyz} = 0,$$

$$\mathcal{F}_{zzz} = 2\mathcal{F}_- + \mathcal{F}_+,$$

$$\mathcal{F}_{zxx} = \mathcal{F}_{zyy} = -\mathcal{F}_- + \mathcal{F}_+. \quad (2.17)$$

Finally, we notice that all the listed terms (2.10)–(2.13), (2.14a), (2.14b), (2.15), and (2.16) remain invariant under the electron-hole ( $e$ - $h$ ) transformation

$$e\text{-}h: \quad \psi \rightarrow \hat{\Sigma}_z \hat{S}_x \psi^*. \quad (2.18)$$

This electron-hole correspondence will be important for the discussion of the instability arising in the in-plane magnetic field, which we will discuss now. (The leading irrelevant term lifting the  $e$ - $h$  symmetry  $\propto \nabla \psi^\dagger \nabla \psi$  does not break any other interesting symmetries and will not be important for our purposes.)

### III. PHYSICAL REASONS FOR THE INSTABILITY AND THE ORDER PARAMETER

Having established the form of the Hamiltonian consistent with the symmetries of the lattice, we turn to the qualitative discussion of the instability and determine the target space of the order parameter. The symmetry arguments will allow us to do this without any actual calculation.

Assume that no symmetries are broken at  $\beta=0$ . Then, the low lying excitations are fermionic electron- and holelike excitations with spin 1/2 and the dispersion  $\epsilon(k) = v(|k|)|k|$ , as shown in Fig. 2(a). The magnetic field parallel to the plane acts only on the spin, and hence, shifts the spectrum of the excitations, making the creation of the Fermi seas for the electrons and holes energetically favorable [Fig. 2(b)]. As the electrons and holes have opposite charges, the Coulomb interaction makes them attract each other. On the other hand, the existence of the finite Fermi surface leads to the Cooper-like instability first discovered in Ref. 11. This instability occurs even for an arbitrary weak interaction potential.

As a result, gap  $\Delta_0(T)$  is formed in the one-particle spectrum [Fig. 2(c)]. The resulting state is an incompressible excitonic insulator with gapped charge excitations. The neutral excitations, however, are still quite interesting.

As the electrons and holes can be paired with different phases, and different valley indices can be involved, the re-

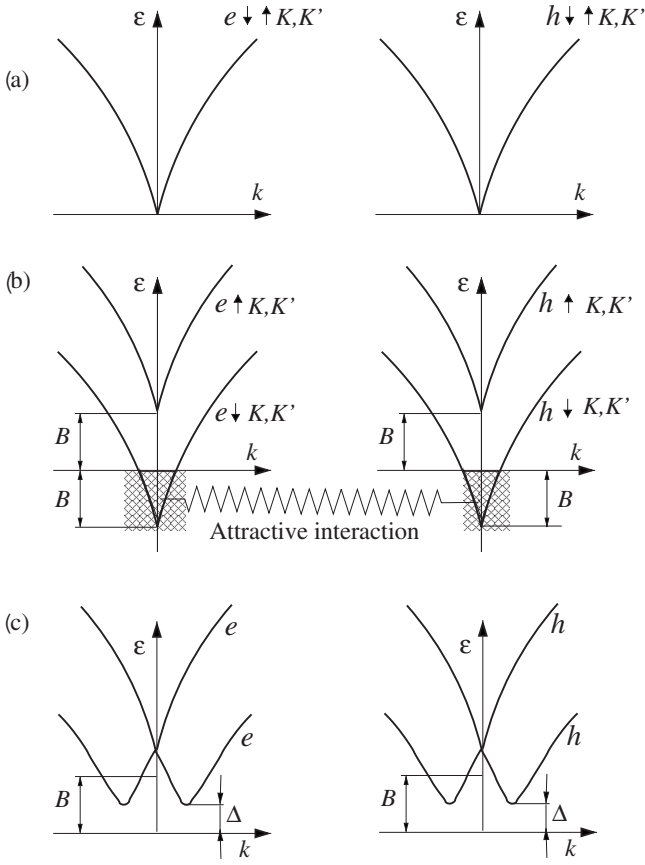


FIG. 2. The mechanism of instability in parallel magnetic field,  $B$ . (a) The spectra of the one-particle excitation at  $B=0$ . (b) The shift of the spectra by finite  $B$  and the formation of the electron and hole Fermi seas. (c) The attractive Coulomb interaction between electrons and holes leads to the instability toward the formation of the excitonic condensate (Ref. 11), creating a gap in the one particle spectrum.

sulting order parameter has a nontrivial matrix structure, which will be discussed now. As the exciton condensate is created by pairing of an electron and a hole with opposite momenta, the order parameter  $\Delta$  has to be of the form  $\langle \psi_e \psi_h \rangle$ . On the other hand, the electron-hole transformation is defined in Eq. (2.18). Thus, we obtain

$$\hat{\Delta} = \langle \psi \otimes \psi^\dagger \rangle = \Delta_0(T) \hat{\Sigma}_z \hat{S}_x. \quad (3.1)$$

Here,  $\Delta$  is an  $8 \times 8$  matrix acting in the space discussed after Eq. (2.3), and the  $\hat{\Sigma}_z$  and  $\hat{S}_x$  are defined in Eq. (2.6).

If only symmetric terms (2.10) and (2.11) were present, the energy of the system would be invariant with respect to the replacement  $\Delta \rightarrow \hat{U} \Delta \hat{U}^\dagger$ , where  $\hat{U}$  is given by Eq. (2.12c). Using Eqs. (3.1) and (2.12c), we obtain the most general form of the matrix order parameter

$$\hat{\Delta} = \Delta_0(T) \hat{\tau}_z^{AB} \otimes \hat{Q}, \quad (3.2a)$$

where  $\hat{Q}$  is the  $4 \times 4$  Hermitian matrix acting in spin and valley spaces subjected to the following constraints:

$$\hat{Q} = \hat{Q}^\dagger; \hat{Q}^2 = \hat{1}^{KK'} \otimes \hat{1}^{AB}; (\hat{1}^{KK'} \otimes \hat{\tau}_z^y) \hat{Q} (\hat{1}^{KK'} \otimes \hat{\tau}_z^y) = -\hat{Q}. \quad (3.2b)$$

The corresponding mean-field single particle spectrum consists of four branches [see Fig. 2(c)]:

$$E_\pm^2 = [\epsilon(k) \pm B]^2 + |\Delta|^2. \quad (3.2c)$$

In terms of the angles in Eq. (2.12c), the  $Q$  matrix can be rewritten as ( $\alpha_-, \mathbf{n}_2 \rightarrow \alpha, \mathbf{n}$ )

$$\hat{Q} = \hat{1}^{KK'} \otimes (\mathbf{e}_1 \hat{\tau}^x) \cos \alpha + (\mathbf{n} \hat{\tau}^{KK'}) \otimes (\mathbf{e}_2 \hat{\tau}^y) \sin \alpha, \quad (3.2d)$$

where  $\mathbf{e}_{1,2}$  are two mutually orthogonal unit vectors in the plane perpendicular to the spin quantization axis  $\mathbf{e}_1 = (\cos \theta_s, \sin \theta_s, 0)$  and  $\mathbf{e}_2 = (-\sin \theta_s, \cos \theta_s, 0)$ .

Another way to parametrize  $Q$  from Eq. (3.2b) is to write

$$\hat{Q} = \begin{pmatrix} 0 & \hat{V} \\ \hat{V}^\dagger & 0 \end{pmatrix}_s, \quad \hat{V}^\dagger \hat{V} = \hat{1}^{KK'}, \quad (3.2e)$$

where  $\hat{V}$  is a unitary  $2 \times 2$  matrix in the valley space. Therefore, the order parameter is described by  $U(2) = SO(3) \times U(1)$  matrices.

Before writing down the effective action or the free energy functional, it is better to explain the physical meaning of different angles in Eq. (3.2d). To do so we will introduce the spin density and the ‘‘spin flux,’’ which, in terms of the original (not smooth) fermionic fields, have the form

$$\vec{s}(\mathbf{r}) = \frac{1}{2} \langle \Psi_\sigma^\dagger(\mathbf{r}) \vec{\tau}_{\sigma\sigma'}^\sigma \Psi_{\sigma'}(\mathbf{r}) \rangle,$$

$$\vec{\Phi}(\mathbf{r}) = \frac{i}{9} \sum_{j_1, j_2=1}^3 \sin \frac{2\pi j_{12}}{3} \langle \Psi_\sigma^\dagger(\mathbf{r} + \vec{a}_{j_2}) \vec{\tau}_{\sigma\sigma'}^\sigma \Psi_{\sigma'}(\mathbf{r} + \vec{a}_{j_1}) \rangle, \quad (3.3)$$

where the translation vectors  $\vec{a}_{1,2,3}$  are shown in Fig. 1, and  $j_{12} = j_1 - j_2$ .

Using Eqs. (2.1), (3.1), (3.2a), (3.2b), (3.2c), (3.2d), and (3.2e), we find

$$\vec{s}(\mathbf{r}) \propto \mathbf{e}_2 \sin \alpha \{ n_z [ |u_A(\mathbf{r})|^2 - |u_B(\mathbf{r})|^2 ] + 2n_x \text{Re} u_A(\mathbf{r}) u_B(\mathbf{r}) + 2n_y \text{Im} u_A(\mathbf{r}) u_B(\mathbf{r}) \}. \quad (3.4a)$$

The corresponding spin-density configurations consistent with the phase factors of the Bloch function of Figs. 1 are shown in Fig. 3(a)–3(c). The configuration of  $\alpha = \pi/2$ ,  $n_z = 1$  corresponds to the site centered spin-density wave. It does not change the periodicity of the original lattice, so the Bragg peaks in the neutron scattering will remain at the same positions  $\vec{q} = j_1 \vec{b}_1 + j_2 \vec{b}_2$ , and the ordering will affect only their internal structure. On the other hand,  $\alpha = \pi/2$ ,  $n_z = 0$  [see Fig. 3(b) and 3(c)] corresponds to the link centered density waves. It is easy to see that in that case the unit cell is tripled so that additional Bragg peaks at the positions  $\vec{q} = \pm K + j_1 \vec{b}_1 + j_2 \vec{b}_2$  will emerge. Rotation in  $n_x$ - $n_y$  plane corresponds to a smooth transition between Figs. 3(b) and 3(c)

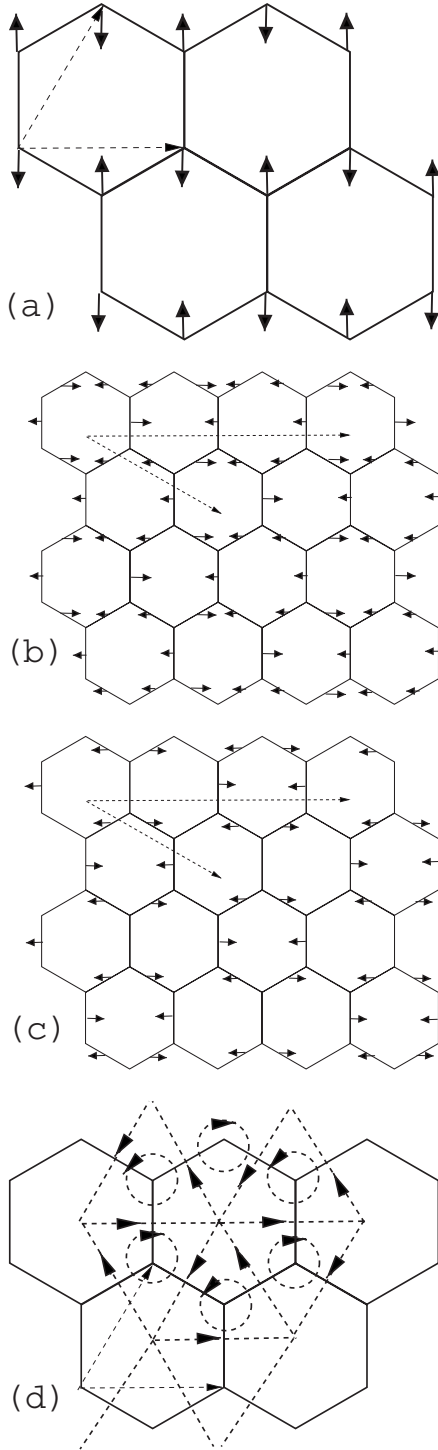


FIG. 3. Sketches of the spin density from Eq. (3.4a), for  $\alpha = \pi/2$  and (a)  $n_z=1$  [ $N_4=1$  in the notation of Eq. (4.5)], (b)  $n_x=1$  ( $N_2=1$ ), and (c)  $n_y=1$  ( $N_3=1$ ). Dashed arrowed lines show the primitive translation vectors of the resulting superstructure. Here, we choose  $\mathbf{e}_2=(1,0,0)$  and  $\mathbf{e}_1=(0,0,1)$ . Notice that the coordinate frame for the spin is rotated with respect to the spatial frame (axis  $x$  for the spin is the direction perpendicular to the plane and  $y$  is in plane whose axis is perpendicular to the magnetic field). (d) Lines of the constant spin flux  $\vec{\Phi}(\mathbf{r}) \cdot \mathbf{e}_1$  (dashed lines) from Eq. (3.4b),  $\alpha=0$  ( $N_1=1$ ). Those lines can be also thought of as the spin current lines.

configurations. Such a smooth rotation can be also understood as a continuous sliding of the superimposed spin-density wave with respect to the crystal lattice.

The spin flux [Fig. 3(d)] is maximal at  $\alpha=0$  and  $\pi$ ,

$$\vec{\Phi}(\mathbf{r}) \propto \mathbf{e}_1 \cos \alpha [ |u_A(\mathbf{r})|^2 - |u_B(\mathbf{r})|^2 ]. \quad (3.4b)$$

Unfortunately, it is not coupled to any obvious physical field, which makes its direct experimental observation unlikely.

#### IV. FREE ENERGY, THERMAL FLUCTUATIONS, AND PHASE DIAGRAM

Order parameter (3.2a), (3.2b), (3.2c), (3.2d), and (3.2e) allows for smooth rotations between all the states of Fig. 3, and thus, is subjected to strong thermal fluctuations. Such fluctuations are governed by the Landau free energy functional, which we are about to describe.

First, we introduce a new definition of  $\Lambda$  and  $S$  matrices [Eq. (2.6)] as

$$\hat{\Lambda}_\alpha = \hat{\gamma}_\alpha^{KK'} \otimes 1^s, \quad \hat{S}_\alpha = 1^{KK'} \otimes \hat{\gamma}_\alpha^s, \quad (4.1)$$

where  $\alpha=x, y$ , and  $z$ , and  $\hat{\Lambda}_\pm \equiv (\hat{\Lambda}_x \pm i\hat{\Lambda}_y)/2$ . This modification is convenient because there are no gapless rotations possible in the sublattice space after the value of the mean-field order parameter is established.

The only possible form for the free energy compatible with the symmetries of the system (2.5) is given by

$$\mathcal{Z} \propto \sum_v \dots \mu^{N_v} \int \mathcal{D}\hat{Q} \exp \left[ -\frac{1}{T} \int d^2\mathbf{r} \mathbf{F}\{\hat{Q}\} \right], \quad (4.2)$$

$$\mathbf{F} = \mathbf{F}_0 + \mathbf{F}_\perp + \mathbf{F}_\triangleright,$$

where  $\sum_v \dots \mu^{N_v}$  stands for a summation over the topological defects (see Sec. IV A) and  $\mu$  denotes a fugacity of such defects. A description of the thermodynamics in terms of matrix  $Q$  subject to hard constraints (3.2b) is valid only at distances larger than the spatial scale

$$\xi_{MF} \approx \frac{v(R_B)}{\Delta_0(T)}, \quad (4.3)$$

where the scale dependence of the velocity and the length  $R_B$  is defined by microscopic theory (see Sec. V D).

The dominant term in the free energy,

$$\mathbf{F}_0 = \frac{1}{8} \left\{ \rho_K(r_0) \text{Tr}(\partial_\nu \hat{Q})^2 + \frac{1}{4} [\rho_s(r_0) - \rho_K(r_0)] \right. \\ \left. \times [-i \text{Tr} \hat{S}_z \hat{Q} \partial_\nu \hat{Q}]^2 \right\} \quad (4.4a)$$

[new notation is defined in Eq. (4.1)], has a symmetry which is higher than the symmetry of the original problem [see Eq. (2.12)]. Hereinafter, we will imply the summation over the repeating index  $\nu=x$  and  $y$ .

To facilitate further analysis, we rewrite Eq. (4.4a) using parametrization (3.2e)



$$\mathbb{F}_\circ = \frac{1}{4} \left\{ \rho_K(r_0) \text{Tr}(\partial_\nu \hat{V}^\dagger \partial_\nu \hat{V}) + \frac{1}{2} [\rho_s(r_0) - \rho_K(r_0)] \right. \\ \left. \times [-i \text{Tr} \hat{V}^\dagger \partial_\nu \hat{V}]^2 \right\}, \quad (4.4b)$$

where  $\hat{V}$  is a unitary  $2 \times 2$  matrix. Further investigation of free energy (4.4a) is postponed until Sec. IV A.

The remaining contributions, though may be small, are crucial because they remove artificial symmetries of the system. The following terms suppress SU(2) rotations in the valley space:

$$\mathbb{F}_\perp = \frac{1}{8r_0^2} \sum_{\alpha=x,y,z} \eta_\alpha(r_0) \text{Tr} \hat{Q} \hat{\Lambda}_\alpha \hat{Q} \hat{\Lambda}_\alpha, \quad \eta_x = \eta_y = \eta_z, \quad (4.4c)$$

$$\mathbb{F}_\square = \frac{\kappa(r_0)}{16r_0^2} \sum_{\alpha,\beta=x,y} \text{Tr} \hat{Q} \hat{\Lambda}_\beta \hat{Q} \hat{\Lambda}_\beta \hat{Q} \hat{\Lambda}_\alpha \hat{Q} \hat{\Lambda}_\alpha. \quad (4.4d)$$

Finally, the term

$$\mathbb{F}_\triangleright = \frac{\zeta(r_0)}{4r_0^2} \text{Tr}[(\hat{Q} \hat{\Lambda}_+)^6 + (\hat{Q} \hat{\Lambda}_-)^6] \quad (4.4e)$$

generated by the umklapp processes reduces the U(1) rotations in the valley space to discrete rotations (2.5d).

A discussion of the role played by anisotropic terms (4.4c) and (4.4e) will be continued in Sec. IV B.

### A. Isotropic part of the action and topological defects

The sum over discrete topological defects can be replaced by a path integral over continuous variables—dual fields. Introduction of dual fields becomes more transparent when one uses the following parametrization of the order parameter (3.2e):

$$V = e^{i\theta_s} g, \quad g = \begin{pmatrix} N_1 + iN_4 & iN_2 + N_3 \\ iN_2 - N_3 & N_1 - iN_4 \end{pmatrix}, \quad (4.5)$$

where  $g$  is an SU(2) matrix and  $\sum_{i=1}^4 N_i^2 = 1$ . Then free energy density (4.4b) acquires the form

$$\mathbb{F}_\circ = \frac{\rho_K}{2} \sum_{i=1}^4 (\partial_\nu N_i)^2 + \frac{\rho_s}{2} (\partial_\nu \theta_s)^2. \quad (4.6)$$

So it appears that the U(1) and SU(2) sectors of the theory are decoupled. This decoupling, however, breaks down when one takes into account the topological defects. As we shall demonstrate, the non-Abelian sector changes the selection rules for the vortex winding numbers.

As usual for compact theories, the free energy density expression obtained in the continuous limit has to be supplemented by topological defects to take into account the behavior of the order parameter in the vicinity of some singular points  $\mathbf{r}_j$ , where it vanishes:  $\hat{Q}^2(\mathbf{r}_j) = 0$ ;  $\hat{V}(\mathbf{r}_j) \hat{V}^\dagger(\mathbf{r}_j) = 0$ . The absolute value of the order parameter is established at the distances of the order of  $\xi_{MF}$  [see Eq. (4.3)] and at large distances, the defect is characterized by a contour integral around it.

The topological defects are characterized by the winding number

$$q = \frac{i}{4\pi} \oint dx_\nu \text{Tr}(V^\dagger \partial_\nu V). \quad (4.7)$$

The most standard approach would be to keep the  $g$  matrix in Eq. (4.5) single valued and nonsingular, and create  $2\pi$ -vortex configuration in U(1) field  $\theta_s$ :

$$e^{i\theta_s} = \frac{(x-x_i) \pm i(y-y_i)}{\sqrt{(x-x_i)^2 + (y-y_i)^2}},$$

$$\frac{1}{2\pi} \oint dx_\nu \partial_\nu \theta_s = \frac{i}{4\pi} \oint dx_\nu \text{Tr}(V^\dagger \partial_\nu V) = \pm 1. \quad (4.8)$$

If only such excitations were present, U(1) and SU(2) sectors would remain decoupled and the standard Berezinskii-Kosterlitz-Thouless (BKT) transition<sup>12,13</sup> would occur in the U(1) sector.

There are, however, other configurations which are energetically more profitable than those of Eq. (4.8). Indeed, consider the configuration of the form

$$\hat{V}_{1/2} = e^{i\mathbf{n} \cdot \hat{\sigma}/2} \begin{pmatrix} \frac{(x-x_i) \pm i(y-y_i)}{\sqrt{(x-x_i)^2 + (y-y_i)^2}} & 0 \\ 0 & 1 \end{pmatrix} e^{-i\mathbf{n} \cdot \hat{\sigma}/2}, \quad (4.9)$$

where  $\mathbf{n}(\mathbf{r})$  is a smooth three-dimensional unit vector  $\sum_{i=1}^3 n_i^2 = 1$ , and  $\hat{\sigma}_i$  are the Pauli matrices.

Rewriting Eq. (4.9) in the form of Eq. (4.5), we obtain, instead of Eq. (4.8),

$$q = \frac{i}{4\pi} \oint dx_\nu \text{Tr}(V^\dagger \partial_\nu V) \pm \frac{1}{2}, \quad (4.10)$$

i.e., configuration (4.9) corresponds to a  $\pi$  or *half-vortex* in the U(1) sector glued with a half-vortex in the SU(2) sector. Since the stiffness in the SU(2) sector vanishes at large distances, the change of sign of  $g$  in large defects does not require energy. So in the absence of anisotropy, the main effect of the SU(2) sector is the change in selection rules of the vortices reflected in their topological invariant (4.7).

To anticipate the role of the vortex and half-vortex configurations in the thermodynamic properties of the system, we evaluate their energies. Substituting configurations (4.8) and (4.9) into Eqs. (4.4b) and (4.6), we find

$$E_{1/2} = \left(\frac{1}{2}\right)^2 \pi(\rho_s + \rho_K) \ln\left(\frac{L}{\xi_{MF}}\right), \\ E_1 = \pi\rho_s \ln\left(\frac{L}{\xi_{MF}}\right), \quad (4.11)$$

where  $L$  is the system size. As  $\rho_K \ll \rho_s$ , one can see that the half-vortices are, in fact, the main configurations responsible for the disordering of the U(1) sector, which we will, in due course, incorporate into the corresponding renormalization group (RG) equations.

To treat the contributions of the topological configurations (4.8) and (4.10) systematically, we rewrite the partition function (4.2) (still neglecting the anisotropic parts) in the form

$$\begin{aligned} \mathcal{Z} &\propto \int D\hat{V}D\hat{h} \exp\left[-\frac{1}{T} \int d^2\mathbf{r} \mathbb{F}\{\hat{V}, \hat{V}^\dagger, \hat{h}\}\right], \\ \frac{\mathbb{F}}{T} &= \frac{1}{4} \text{Tr} \left\{ \frac{\rho_K}{T} \partial_x \hat{V}^\dagger \partial_x \hat{V} + \frac{T}{\rho_K} (\partial_x \hat{h})^2 + 2 \hat{V}^\dagger \partial_y \hat{V} \partial_x \hat{h} \right\} \\ &+ \frac{[\rho_s - \rho_K]}{8T} [-i \text{Tr} \hat{V}^\dagger \partial_x \hat{V}]^2 + \left[ \frac{T}{8\rho_s} - \frac{T}{8\rho_K} \right] [\text{Tr} \partial_x \hat{h}]^2 \\ &- \frac{2\mu_1}{r_0^2} \cos 2\pi h_s - \frac{2\mu_{1/2}}{r_0^2} \frac{\sin \pi |\vec{h}|}{\pi |\vec{h}|} \cos \pi h_s, \\ \hat{V} \hat{V}^\dagger &= 1, \\ \hat{h} = \hat{h}^\dagger &= h_s \mathbb{1}^s + \vec{h} \cdot \hat{\tau}^s, \end{aligned} \quad (4.12)$$

where  $2 \times 2$  matrix  $\hat{h}$  is the dual field,  $\hat{\tau}_{x,y,z}^s$  are the Pauli matrices in the spin space, and  $\mu_1$  and  $\mu_{1/2}$  are fugacities for the vortices and half-vortices, respectively. Though it may appear that Eq. (4.12) breaks the rotational symmetry, all the physical correlation functions calculated using Eq. (4.12) are rotationally symmetric. The derivation of Eq. (4.12) is relegated to Appendix A.

Summing up the leading logarithmic series within the first loop renormalization group scheme, we find the following equations for the corresponding fugacities:

$$\frac{d\mu_{1/2}}{d \ln r_0} = \left[ 2 - \left( \frac{1}{2^2} \right) \frac{\pi}{T} (\rho_K + \rho_s) \right] \mu_{1/2}. \quad (4.13a)$$

They are valid for  $\mu_{1/2}, \mu \ll 1$  and also  $\rho_K \gg T$ .

The fugacity for the conventional vortices evolves as

$$\frac{d\mu_1}{d \ln r_0} = \left( 2 - \frac{\pi \rho_s}{T} \right) \mu_1 \quad (4.13b)$$

for  $\mu_1 \ll 1$ . Equations (4.13a) and (4.13b) are analogous for the simple estimate of the energy of the defects (4.11); however, they allow for a renormalization of the stiffness  $\rho_s$  caused by the bound pairs of (half)vortices and (half)antivortices, and of the stiffness  $\rho_K$  caused by the bound pairs of half-vortices and anti-half-vortices, as well as by thermal fluctuations of the order parameter. The latter renormalization, for  $\mu_{1/2}, \mu \ll 1$  and  $\rho_K \gg T$ , can be represented in the form

$$\frac{d\rho_K}{d \ln r_0} = -\frac{T}{\pi} - \mu_{1/2}^2 \beta_K^{(1/2)}(\rho_K, \rho_s), \quad (4.14a)$$

$$\frac{d\rho_s}{d \ln r_0} = -\mu_{1/2}^2 \beta_s^{(1/2)}(\rho_K, \rho_s) - \mu_1^2 \beta_s^{(1)}(\rho_s). \quad (4.14b)$$

Functions  $\beta$  in Eqs. (4.14a) and (4.14b) are difficult to obtain explicitly for arbitrary stiffnesses. However, such forms will not be necessary for further consideration.

As the initial fugacities of the half-vortices  $\mu_{1/2}$  are not much smaller than the fugacities for the vortices  $\mu_1$ , the latter ones being less relevant can be neglected in the description of the phase transition. In the limit of  $\mu_{1/2} \ll 1$ , one can

also neglect the half-vortices in the renormalization of  $\rho_K$ . Then, from Eq. (4.14a), we obtain the following equations:

$$\rho_K(r_0) = \frac{T}{\pi} \ln \frac{\xi_K}{r_0}, \quad \xi_K = \xi_{MF} \exp\left(\frac{\pi \rho(\xi_{MF})}{T}\right), \quad (4.15)$$

for  $\xi_{MF} \lesssim r_0 \lesssim \xi_K$ . At  $r_0 \sim \xi_K$ , the perturbative renormalization group is no longer valid, and the SU(2) sector enters into the strongly disordered regime. Hence, length  $\xi_K$  is the correlation length of the order parameter.

At  $r_0 \gg \xi_K$ , the non-Abelian stiffness vanishes:  $\rho_K \rightarrow 0$ . We can then use Eq. (4.13a) to obtain the value of the Kosterlitz jump at the phase transition:

$$\frac{\pi \rho_s(T_{KT} - 0)}{T} = 2 * 2^2. \quad (4.16a)$$

This value is modified in comparison with the pure U(1) model

$$\frac{\pi \rho_s(T_{KT} - 0)}{T} = 2 \quad (4.16b)$$

due to the presence of half-vortices and the SU(2) sector being disordered.

Assuming that  $\mu_{1/2}(\xi_{MF}) \ll 1$ , we can also use Eq. (4.16a) to estimate  $T_{KT}$ :

$$\frac{\pi \rho_s(T_{KT})}{2T_{KT}} = 2^2 + \mathcal{O}[\mu_{1/2}(\xi_{MF})]. \quad (4.17)$$

In Sec. V, we will use Eq. (4.17) to relate  $T_{KT}$  to the mean-field transition temperature  $T_{MF}$ .

The main conclusions of these sections are the following: (i) spin U(1) and valley SU(2) rotations are coupled to each other in the presence of half-vortices, and (ii) the U(1) sector acquires the algebraic order at  $T < T_{KT}$ , whereas the isotropic version of the valley rotations always remain disordered.

The purpose of the next two sections is to analyze how the disorder in the valley space is affected when the artificial symmetries are lifted by the leading anisotropies.

## B. Effect of weak anisotropies

Let us assume that the BKT transition in the U(1) sector has already occurred so that the half-vortices are not relevant, and SU(2) sector is decoupled. (This assumption will be lifted in Sec. IV C.) Then the thermal fluctuations lead to the renormalization of the anisotropies in the same fashion as the first term in the right-hand side of Eq. (4.14a). In the first loop approximation, we find

$$\begin{aligned} \frac{d\eta_\alpha}{d \ln r_0} &= \left[ 2 - \frac{2T}{\pi \rho_K} \right] \eta_\alpha, \\ \frac{d\kappa}{d \ln r_0} &= \left[ 2 - \frac{8T}{\pi \rho_K} \right] \kappa, \\ \frac{d\zeta}{d \ln r_0} &= \left[ 2 - \frac{12T}{\pi \rho_K} \right] \zeta. \end{aligned} \quad (4.18)$$





The derivation of Eq. (4.26) is completely analogous to the derivation of Eq. (4.12) (see also Appendix A.)

The first loop scaling equations for the anisotropy  $\eta_{\perp}$  and the vortex fugacities  $\mu_{14}$  are

$$\begin{aligned} \frac{d\mu_{14}}{d \ln r_0} &= \left(2 - \frac{\pi\rho_K}{T}\right) \mu_{14}, \\ \frac{d\eta_{\perp}}{d \ln r_0} &= \left(2 - \frac{T}{\pi\rho_K}\right) \eta_{\perp}. \end{aligned} \quad (4.27)$$

They have the obvious solutions

$$\begin{aligned} \mu_{14}(r_0) &= \mu_{14}(R_*) \left(\frac{R_*}{r_0}\right)^{(\pi\rho_K - 2T)/T}, \\ \eta_{\perp}(r_0) &= \eta_{\perp}(R_*) \left(\frac{R_*}{r_0}\right)^{(T - 2\pi\rho_K)/\pi\rho_K}. \end{aligned} \quad (4.28)$$

If  $\eta_{\perp}(R_*)=0$ , the system undergoes Berezinskii-Kosterlitz-Thouless transition at  $T_{BKT}=\pi\rho_K/2$ , from the high temperature vortex-dominated disordered state to a phase with power law correlations.

At nonzero  $\eta_{\perp}$ , the ordered phase has a finite correlation length since below  $\pi\rho_K/2$  the anisotropy  $\eta_{\perp}$  is a relevant perturbation. Therefore, phase  $\phi$  is locked and the system is ordered with a finite correlation length  $\xi_{14}$  determined by the condition  $\eta_{\perp}(\xi_{14}) \simeq T$  so that

$$\xi_{14} \simeq R_* \left(\frac{T}{\eta_{\perp}(R_*)}\right)^{\pi\rho_K/(2\pi\rho_K - T)}. \quad (4.29)$$

From Eq. (4.29), one may conclude that the transition between phases (I) and (II) of Fig. 4 is a continuous one, with smoothly varying correlation length exponent along the transition line. However, we will see shortly that this conclusion is an artifact of neglecting the higher order anisotropy (4.4d).

At temperatures above  $\pi\rho_K/2$ , both the anisotropy (order) and the vortices (disorder) are relevant. The corresponding operators compete with each other since  $\theta$  and  $\phi$  cannot be locked simultaneously. To estimate the location of the transition line and the length scale  $\xi_I$  at which criticality becomes important, we require

$$\frac{\eta_{\perp}(\xi_I)}{T} \simeq \mu_{14}(\xi_I) \simeq 1,$$

which yields, assuming as usual that  $\mu_{14}(R_*) \ll 1$ ,

$$\begin{aligned} \xi_I &\simeq R_* \left(\frac{1}{\mu_{14}(R_*)}\right)^{T/(2T - \pi\rho_K)}, \\ \eta_c(\rho_K) &= T[\mu_{14}(R_*)]^{(T/\pi\rho_K)(2\pi\rho_K - T)/(2T - \pi\rho_K)}. \end{aligned} \quad (4.30)$$

At distances larger than  $\xi_I$ , the anisotropy is the largest scale in the problem, so that  $N_1(N_4)$  becomes massive and the vortices provide the possibility for  $N_4^2(N_1^2)$  to change on the scale of the order of  $\xi_I$ . The resulting transition, therefore, involves only one soft mode, and thus, belongs to the Ising model universality class (see Appendix B for more accurate calculation in the vicinity of  $\pi\rho_K=T$ ). The corresponding correlation length  $\xi$  is, then, given by

$$\xi \simeq \xi_I \frac{\eta_{\perp}^c}{|\eta_{\perp} - \eta_{\perp}^c|}, \quad |\eta_{\perp} - \eta_{\perp}^c| \simeq \eta_{\perp}^c. \quad (4.31)$$

So far, we ignored the higher order anisotropy term. In fact, those terms are important only in the vicinity of (I)-(II) transition line, where they change the order of the phase transition.

To see this, we rewrite Eq. (4.4d) using parametrizations (3.2e) and (4.5):

$$\frac{F_{\square}}{T} = \frac{\kappa(R_*)}{TR_*^2} \text{Re}(N_x + iN_y)^4 = \frac{\kappa(R_*)}{TR_*^2} \cos 4\phi. \quad (4.32)$$

Equation (4.32) should be added to Eq. (4.26).

The coupling in Eq. (4.32) is renormalized by thermal fluctuations. The first loop RG equation and its solution are given by

$$\begin{aligned} \frac{d\kappa}{d \ln r_0} &= \left(2 - \frac{4T}{\pi\rho_K}\right) \kappa, \\ \kappa(r_0) &= \kappa(R_*) \left(\frac{R_*}{r_0}\right)^{(4T - 2\pi\rho_K)/\pi\rho_K}. \end{aligned} \quad (4.33)$$

At  $\pi\rho_K > 2T$ , the quartic anisotropy  $\kappa$  is a relevant perturbation, so that the phase  $\phi$  becomes locked, and the system is ordered in locally stable state even for  $\eta_{\perp}=0$ , so that the correlation length  $\xi_{14}$  is always limited by  $\tilde{\xi}_{14}$ , which is found from the condition  $\kappa(\tilde{\xi}_{14}) \simeq T$ . It yields

$$\xi_{14} \simeq \tilde{\xi}_{14} \simeq R_* \left(\frac{T}{|\kappa(R_*)|}\right)^{\pi\rho_K/(2\pi\rho_K - 4T)}. \quad (4.34)$$

The length  $\tilde{\xi}_{14}$  diverges when the approaching the multicritical point  $\pi\rho_K=2T$ ,  $\eta_{\perp}=0$ . At length scale large than  $\tilde{\xi}_{14}$ , the nonvanishing order parameter is found by minimization of the expression

$$\frac{\tilde{F}}{T} = \frac{\eta_{\perp}(\tilde{\xi}_{14})}{\tilde{\xi}_{14}^2 T} \cos 2\phi + \text{sgn } \kappa \cos 4\phi \quad (4.35)$$

with respect to  $\phi$ , which produces two second order (Ising type) phase transitions for  $\kappa > 0$ , and the first order phase transition for  $\kappa < 0$  [in the former case,  $\tilde{\xi}_{14}$  serves as prefactor for the diverging correlation length similarly to Eq. (4.31)].

At  $\pi\rho_K < 2T$ , the quartic anisotropy becomes irrelevant and we obtain from Eqs. (4.33) and (4.30)

$$\kappa(\xi_I) = \kappa(R_*) \left(\frac{1}{\mu_{14}}\right)^{2/\pi\rho_K} < T, \quad (4.36)$$

i.e., it cannot affect the position and the universality class of the Ising phase transitions.

The resulting structure of the phase diagram in the vicinity of the line  $\eta_{\perp}=0$ ,  $\eta_z < 0$  is summarized in Fig. 5.

## 2. Vicinity of the lines $\eta_z > 0$ , $\eta_{\perp} = \pm \eta_z$

In the vicinity of the line  $\eta_z > 0$ ,  $\eta_{\perp} = -\eta_z$ , anisotropy (4.24) generates mass for the field  $N_4$  so that the free energy

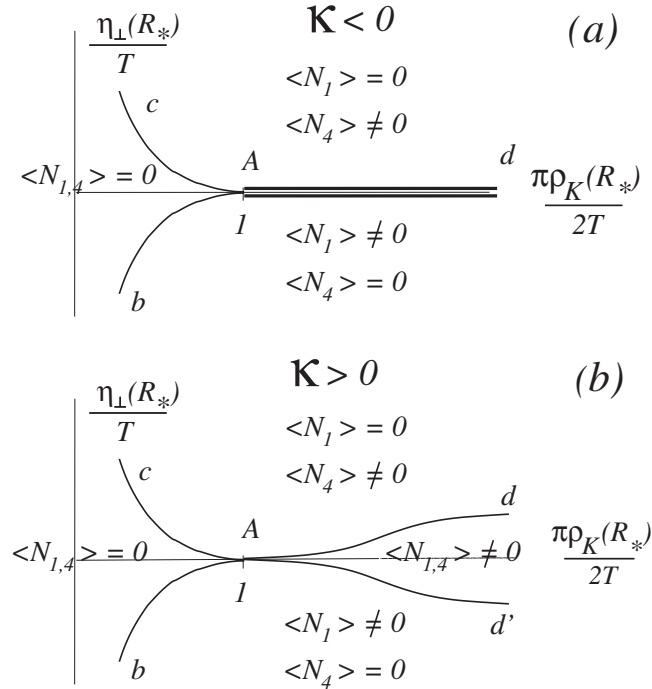


FIG. 5. Phase diagrams in the vicinity of the line  $\eta_{\perp}=0$ ,  $\eta_z < 0$ . Lines A-b and A-c are always of the Ising type. (a) Line A-d is (weak) first order phase transition line at  $\kappa < 0$ . (b) Lines A-d and A-d' are second order phase transitions (Ising type) at  $\kappa > 0$ . At  $\kappa = 0$ , the A-d line is a continuous phase transition, with the varying indices given by Eq. (4.28).

for the remaining soft modes [see Eqs. (4.6) and (4.4e)] is

$$\mathbb{F} = \frac{\rho_K(R_*)}{2} \sum_{i=1}^3 (\partial_i N_i)^2 + \frac{\Delta \eta(R_*)}{R_*^2} N_1^2 + \frac{\zeta(R_*)}{R_*^2} \text{Re}(N_2 + iN_3)^6,$$

$$N_1^2 + N_2^2 + N_3^2 = 1,$$

$$\Delta \eta(R_*) \equiv \eta_z(R_*) + \eta_{\perp}(R_*), \quad (4.37)$$

where length scale  $R_*$  and the coupling constants are defined in Eqs. (4.22), (4.15), and (4.19). The vicinity of the line  $\eta_z > 0$ ,  $\eta_{\perp} = \eta_z$  does not require a separate consideration as it is also described by the free energy density (4.37) after the replacement

$$N_1 \rightarrow N_4, \quad \eta_{\perp}(R_*) \rightarrow -\eta_{\perp}(R_*). \quad (4.38)$$

At  $r_0 > R_*$ , the scaling of the couplings in Eq. (4.37) is governed by the first loop renormalization group equations

$$\frac{d\rho_K}{d \ln r_0} = -\frac{T}{2\pi}, \quad (4.39a)$$

$$\frac{d\Delta \eta}{d \ln r_0} = \left[ 2 - \frac{3T}{2\pi\rho_K} \right] \Delta \eta, \quad (4.39b)$$

$$\frac{d\zeta}{d \ln r_0} = \left[ 2 - \frac{21T}{2\pi\rho_K} \right] \zeta, \quad (4.39c)$$

where we neglect the effect of the anisotropies on the renormalization of the stiffness, which, however, will be sufficient for our purposes.

The solution of Eq. (4.39a) is

$$\rho_K(r_0) = \frac{T}{2\pi} \ln \frac{\xi_H}{r_0}, \quad \xi_H = R_* \exp\left(\frac{2\pi\rho(R_*)}{T}\right), \quad (4.40a)$$

which is consistent with the well known fact that the classical SU(2)/U(1) sigma model is always disordered by the thermal fluctuations, with  $\xi_H$  being the correlation length for these fluctuations.

Anisotropies may lead to ordering. To estimate the positions of the phase transition lines, we solve Eqs. (4.39b) and (4.39c) with the help of Eq. (4.40a) and find

$$\Delta \eta(r_0) = \Delta \eta(R_*) \left(\frac{r_0}{R_*}\right)^2 \left(\frac{\ln \frac{\xi_H}{r_0}}{\ln \frac{\xi_H}{R_*}}\right)^3,$$

$$\zeta(r_0) = \zeta(R_*) \left(\frac{r_0}{R_*}\right)^2 \left(\frac{\ln \frac{\xi_H}{r_0}}{\ln \frac{\xi_H}{R_*}}\right)^{21}. \quad (4.40b)$$

First, let us neglect the hexadic anisotropy,  $\zeta=0$ . Then, the anisotropy is important if  $|\Delta \eta(r_0 \approx 2\xi_H)| > T$ . Equations (4.40b) and (4.40a) give us approximate positions of the phase transition lines

$$\frac{\Delta \eta_{\perp}(R_*)}{T} = \left(\alpha_{\perp} \frac{2\pi\rho_K(R_*)}{T}\right)^3 \exp\left(-\frac{4\pi\rho_K(R_*)}{T}\right),$$

$$\frac{\Delta \eta_l(R_*)}{T} = -\left(\alpha_l \frac{2\pi\rho_K(R_*)}{T}\right)^3 \exp\left(-\frac{4\pi\rho_K(R_*)}{T}\right), \quad (4.41)$$

shown in Fig. 6. The numerical prefactors  $\alpha_{l,\perp}$  of order unity cannot be obtained within a perturbative RG scheme.

Line  $\Delta \eta_l$  corresponds to the second order phase transition from the disordered phase to the phase characterized by  $\langle N_l \rangle \neq 0$ . This phase transition belongs to the universality class of the two-dimensional Ising model. Additional hexadic anisotropy (finite but small  $\zeta$ ) cannot affect this transition.

Line  $\Delta \eta_{\perp}$  corresponds to the phase transition from the disordered phase to the phase characterized by algebraic correlations for  $N_{2,3}$ , i.e., to the Berezinskii-Kosterlitz-Thouless transition. Contrary to the Ising transition, the hexadic term may cause a further ordering and an additional Berezinskii-Kosterlitz-Thouless type transition between the algebraically ordered phase and the long-range ordered phase.

To describe those two transitions, we put  $N_1=0$  in Eq. (4.37) and introduce the field  $\phi$ , so that  $N_2 = \cos \phi$  and  $N_3$

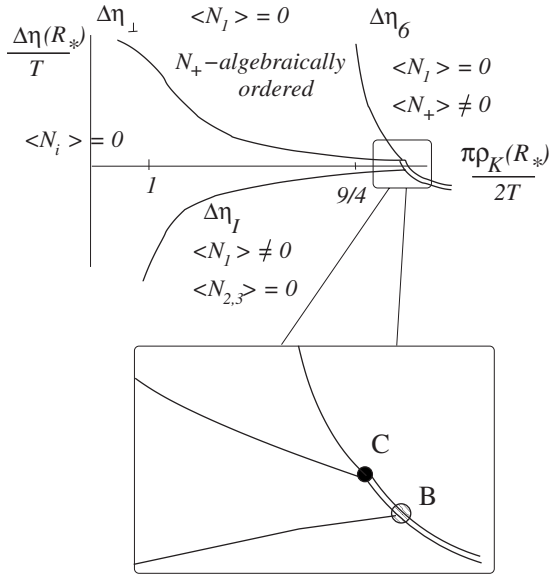


FIG. 6. Phase diagrams in the vicinity of the line  $\Delta\eta = \eta_z + \eta_\perp = 0$ ,  $\eta_z > 0$ . Here,  $N_+ = N_2 + iN_3$ . Lines  $\Delta\eta_{\perp,6}$  are the Berezinskii-Kosterlitz-Thouless phase transitions. Line  $\eta_I$  is the Ising-type phase transition. The double line is the first order phase transition. Point C is the bicritical point and point B is the critical end point.

$= \sin \phi$ , and the dual field  $\theta$  to describe the vortices.

The singular part of the partition function is given by

$$\mathcal{Z} \propto \int \mathcal{D}\phi \mathcal{D}\theta \exp\left(-\frac{\mathbb{F}_{23}}{T}\right),$$

$$\begin{aligned} \frac{\mathbb{F}_{23}}{T} &= \frac{\rho_K}{2T} (\partial_x \phi)^2 + \frac{T}{2\rho_K} (\partial_x \theta)^2 + i \partial_x \theta \partial_y \phi + \frac{\zeta}{R_\perp^2 T} \cos 6\phi \\ &+ \frac{\mu_{23}}{R_\perp^2} \cos(2\pi\theta), \end{aligned} \quad (4.42)$$

where the coupling constant are described by Eqs. (4.15) and (4.40b), and  $R_\perp < R_H$  is found from the requirement  $\rho_K(R_\perp) \approx \Delta\eta(R_\perp)$ . This yields

$$\frac{R_\perp}{\xi_H} \ln \frac{R_\perp}{\xi_H} = \left( \frac{\Delta\eta_\perp(R_*)}{\alpha_\perp^3 \Delta\eta(R_*)} \right)^{1/2}. \quad (4.43)$$

Once again, the scaling of the vortex fugacity  $\mu_{23}$  and of the hexadic anisotropy  $\zeta$  can be determined from the first loop renormalization group equations

$$\frac{d\mu_{23}}{d \ln r_0} = \left[ 2 - \frac{\pi\rho_K}{T} \right] \mu_{23}, \quad (4.44a)$$

$$\frac{d\zeta}{d \ln r_0} = \left[ 2 - \frac{9T}{\pi\rho_K} \right] \zeta. \quad (4.44b)$$

In the limit of  $\mu_{23}, \zeta \ll 1$ , Eqs. (4.44a) and (4.44b) enable us to refine the definitions of  $\alpha_\perp$  [requiring  $\pi\rho_K(R_\perp) = 2T$ ] and to find the boundary of the ordered phase  $\eta_6(R_*)$  [requiring  $\pi\rho_K(R_\perp) = 9T/2$ ]. With the help of Eqs. (4.43) and (4.40a), we find

$$\alpha_\perp \approx \frac{e^2}{2^{4/3}} \approx 2.9,$$

$$\eta_6 \approx \left( \frac{4e^9}{9e^4} \right)^2 \eta_\perp \approx 4.3 \times 10^3 \eta_\perp, \quad (4.45)$$

i.e., even though the boundaries of the two phases have the same functional form, they are very well separated due to numerical reasons.

In the previous discussion, we implied that  $\zeta(R_\perp) \ll 1$ . This condition is clearly violated on the lines  $\eta_6$ ,  $\eta_\perp$ , and  $\eta_I$  if  $\pi\rho_K/T \rightarrow \infty$  [see the second equation of Eqs. (4.40a) and (4.40b)]. The large power of the logarithm allows one to use the saddle point expression, and we obtain from condition  $\zeta(R_\perp) \geq 1$ :

$$\frac{\pi\rho(R_*)}{2T} > \frac{21}{8} + \left( \frac{21}{32} \ln \frac{T}{\zeta(R_*)} \right)^{1/2}. \quad (4.46)$$

At larger stiffness, the phase transition occurs by the locking of the order parameter due to the hexadic term, and the fluctuations become unimportant. Minimizing the potential part of the free energy (4.37), we obtain a first order phase transition at  $\eta(R_*) \approx \zeta(R_*)$ .

The only way of connecting the critical lines on the phase diagram, allowed by the symmetries of the system, is shown in the inset of Fig. 6.

### C. Effect of strong anisotropies

In Sec. IV B, we assumed that U(1) sector was ordered and the half-vortices were not important in ordering the SU(2) sector. It was justified by the assumption of the weak enough anisotropy so that the parameter  $\bar{\eta}$  [see Eq. (4.21) is constrained by  $\bar{\eta}(\xi_{MF}) \ll T$ . In this case, the renormalization of the stiffness  $\rho_K$  is so strong that  $\rho_K(R_*) \ll \rho_s$  [see Eq. (4.22)] and separation of the scale was justified. We will see, however, in Sec. V D that for some ranges of the in-plane magnetic field, the opposite limits of the strong anisotropies,  $\bar{\eta}(\xi_{MF}) \geq T$ , are more relevant.

In this case, the logarithmic renormalization of the stiffness  $\rho_K$  [see Eq. (4.14a)] and of the anisotropy parameters [see Eq. (4.18)] are no longer strong and one has to investigate the soft modes in Eq. (4.24) already on the scale of the order of  $\xi_{MF}$ . Similar to the approach of Sec. IV B, only the lines of extra degeneracies require further investigation. The difference is that U(1) sector and the half-vortex configurations have to be taken into account. To simplify further manipulations, we introduce the parameter

$$\gamma \equiv \frac{\rho_K(R_*)}{\rho_s(R_*)} < 1. \quad (4.47)$$

All the results of the previous section correspond to the limiting case  $\gamma \rightarrow 0$ .

#### 1. Vicinity of line $\eta_\perp = 0$ , $\eta_z < 0$

Let us generalize Eq. (4.26) by including the half-vortices. Substituting parametrization (4.5) with  $N_{2,3} = 0$ ,  $N_1$

$=\cos \phi$ , and  $N_4=\sin \phi$  into Eq. (4.12), representing  $2\hat{h}=\text{diag}[\theta+h_s; \theta-h_s]$ , we obtain

$$\mathcal{Z} \propto \int \mathcal{D}\phi \mathcal{D}\theta \mathcal{D}\phi_s \mathcal{D}\theta_s \exp\left(-\frac{\mathbb{F}_{14}}{T}\right),$$

$$\frac{\mathbb{F}_{14}}{T} = \left[ \frac{\rho_K}{2T} (\partial_x \phi)^2 + \frac{T}{2\rho_K} (\partial_x \theta)^2 + i\partial_x \theta \partial_y \phi + \frac{\mu_{14}}{R_*^2} \cos(2\pi\theta) \right. \\ \left. + \frac{\eta_\perp}{R_*^2 T} \cos 2\phi \right] + \left[ \frac{\rho_K}{2\gamma T} (\partial_x \theta_s)^2 + \frac{T\gamma}{2\rho_K} (\partial_x h_s)^2 \right. \\ \left. + i\partial_x h_s \partial_y \theta_s + \frac{\mu_1}{R_*^2} \cos(2\pi h_s) \right] + \frac{\mu_{1/2}}{R_*^2} \cos(\pi h_s) \cos(\pi\theta) \quad (4.48)$$

[procedure to obtain  $\mu_{14}$  term by generating vortices is completely analogous to Eq. (4.26)]. Here,  $\gamma$  is given by (4.47),  $\mu_{14}$  is a fugacity for the creation of a vortex in  $\phi$  field (we will call them “ $N_1-N_4$  vortices”), the vortices in  $\theta_s$  field [we will call them “vortices in the U(1) sector”] are governed by the fugacity  $\mu_1$ , and  $\mu_{1/2}$  is the fugacity for the half-vortices.

The first loop RG equations are analogous to Eqs. (4.13a), (4.13b), and (4.27):

$$\frac{d\mu_{1/2}}{d \ln r_0} = \left[ 2 - \frac{\pi\rho_K}{4T} \left( \frac{1+\gamma}{\gamma} \right) \right] \mu_{1/2},$$

$$\frac{d\mu_{14}}{d \ln r_0} = \left( 2 - \frac{\pi\rho_K}{T} \right) \mu_{14},$$

$$\frac{d\mu_1}{d \ln r_0} = \left( 2 - \frac{\pi\rho_K}{\gamma T} \right) \mu_1,$$

$$\frac{d\eta_\perp}{d \ln r_0} = \left( 2 - \frac{T}{\pi\rho_K} \right) \eta_\perp. \quad (4.49)$$

We will see that  $\gamma=1/4$  is a special point where the  $N_1-N_4$  vortices have the same scaling dimension as the half-vortices for the disordered valley sector. Another special point is  $\gamma=1/3$ , where the half-vortices become more relevant in the disordering of the  $N_1-N_4$  sector than the simple vortices.

The phase diagram for  $\gamma < 1/4$  is shown in Fig. 7. The physics in the vicinity of the multicritical point A is still determined by  $N_1-N_4$  vortices, whereas the half-vortices are irrelevant in this region. Inside the  $N_1-N_4$  disordered region, any deformation in  $\phi$  causes only a finite energy,

$$\langle \cos \pi\theta \rangle \neq 0.$$

Therefore, the half-vortices in U(1) sector are allowed and the condition (4.16a) determines the value of the Kosterlitz jump. In fact,  $\cos \pi\theta$  is proportional to the disorder operator  $\mu$  of the Ising model (see Ref. 14). We will use this analogy shortly.

On the other hand, deep in the ordered sector, the half-vortices are confined and the disordering of the U(1) sector occurs due to the vortices and, thus, the Kosterlitz jump is determined by Eq. (4.16b).

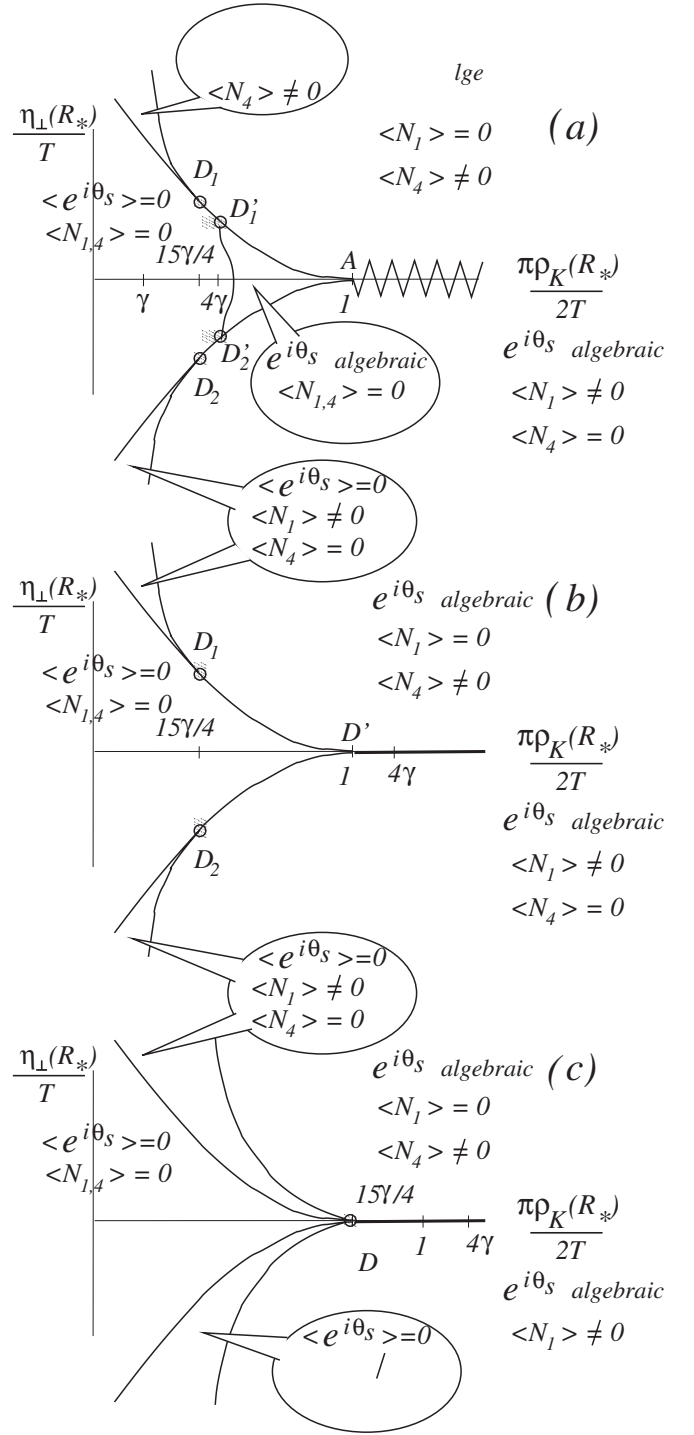


FIG. 7. The phase diagram in the vicinity of the line  $\eta_\perp=0$  for different values of  $\gamma$ . (a)  $\gamma < 1/4$ ; the zigzag line denotes either the first order phase transition or pair of the Ising transition (see Fig. 5). The asymptotics of the Berezinskii-Kosterlitz-Thouless lines are given by Eqs. (4.53) and (4.56) for points  $D_{1,2}$  and  $D'_{1,2}$ , respectively. (b)  $1/4 < \gamma < 4/15$ ; the asymptotics of the Berezinskii-Kosterlitz-Thouless lines are given by Eqs. (4.53) for points  $D_{1,2}$ . (c)  $1/3 < \gamma < 1/4$ . The difference between the slopes of the Ising line and the Berezinskii-Kosterlitz-Thouless line near multicritical point B is given by Eq. (4.53). Finite  $\kappa$  leads to the modification of the multicritical point B.

Only the vicinities of the tricritical points  $D_{1,2}$  and  $D'_{1,2}$  in Fig. 7(a) deserve a special consideration. In their vicinity,  $\mu_1$  term in Eq. (4.48) is irrelevant, and  $\mu_{14}$  and  $\eta_\perp$  terms conspire to produce an Ising critical point. Therefore, at  $\mu_{1/2} = 0$ , we have two decoupled critical theories: the Ising one described by  $\phi, \theta$  fields and the U(1) model described by  $(\theta_s, h_s)$  fields. At the Ising model critical point, the operator  $\cos \theta$  behaves as the disorder parameter field of the Ising model and has scaling dimension  $1/8$ . Hence, the corresponding RG equation for  $\mu_{1/2}$  is

$$\frac{d\mu_{1/2}}{d \ln r_0} = \left[ 2 - \frac{1}{8} - \frac{\pi \rho_s(r_0)}{4T} \right] \mu_{1/2}, \quad (4.50)$$

where we restored  $\rho_s$  using Eq. (4.47).

The scale invariance requirement for the fugacity  $\mu_{1/2}$  gives the stiffness at the multicritical points  $D_{1,2}$

$$\frac{\pi \rho_s^c(r_0 \rightarrow \infty)}{2T_c} = \frac{15}{4} < 4. \quad (4.51)$$

If  $\rho_s < \rho_s^c$ , the half-vortex fugacity  $\mu_{1/2}$  grows according to Eq. (4.50) as

$$\frac{\mu_{1/2}(r_0)}{\mu_{1/2}(R^*)} = \left( \frac{r_0}{R^*} \right)^{15(\rho_s^c - \rho_s)/8\rho_s^c} \quad (4.52)$$

The growth (4.52) has to be stopped at the correlation length of the Ising transition

$$\xi_I \approx \frac{\eta_\perp^c}{|\eta_\perp - \eta_\perp^c|}.$$

At the lengths larger than  $\xi_I$ , the Ising model becomes ordered, so the half-vortices are confined. However, their fusion produces usual vortices with the fugacity  $\mu_1 \approx \mu_{1/2}^2(\xi_I)$ . The requirement for the resulting parameters of the remaining U(1) theory to be on the line of the Berezinskii-Kosterlitz-Thouless transition leads to the estimate  $\mu^{1/2}(\xi_I) \approx 1$  or [see also Fig. 5(a)]

$$\ln \frac{\eta_c}{\eta_\perp^{KT} - \eta_\perp^c} = \frac{8\rho_s^c}{15(\rho_s^c - \rho_s)} + \mathcal{O}(1). \quad (4.53)$$

For the spin stiffnesses, in the interval

$$\rho_s^c < \rho_s < \rho_s^{c,2}, \quad \frac{\pi \rho_s^{c,2}}{2\pi} = 4, \quad (4.54)$$

the fugacity for the half-vortices (4.52) vanishes at  $r_0 \rightarrow \infty$ . If one tries to deviate from the line  $\eta = \eta_c$  toward the ordered side, those half-vortices fuse into vortices which are also irrelevant.

Let us now consider the deviation from the tricritical point toward the disordered side of the Ising sector. In this region,  $\cos \theta$  can be replaced by its average. As we have mentioned above, near the Ising model critical line,  $\cos \theta \sim \mu$  (the disorder operator of the Ising model). Hence, we find

$$\cos \pi \theta \cos \pi h_s \rightarrow |\eta_\perp - \eta_\perp^c|^{1/8} \cos \pi h_s. \quad (4.55)$$

The latter operator is irrelevant in the region (4.54) as well. Therefore, the line  $\eta = \eta_c$ ,  $\rho_s^c < \rho_s < \rho_s^{c,2}$ , is the transition line both for the valley and the spin sectors.<sup>15</sup>

At  $\rho > \rho_s^{c,2}$ , the half-vortices in limit of zero fugacity  $\mu_{1/2}$  become irrelevant and U(1) sector is algebraically ordered. The correction to the vertical line can be evaluated using

$$\rho_s - \rho_s^{c,2} \approx \mu_{1/2}(\xi_I) \propto |\eta_\perp - \eta_\perp^c|^{1/8}. \quad (4.56)$$

This estimate is valid near points  $D'_{1,2}$ .

The case  $\gamma > 1/4$  needs further investigation as the critical points  $D'_{1,2}$  cross the point A [see Figs. 7(b) and 7(c)]. For simplicity, we will neglect the quartic anisotropies:  $\kappa = 0$ .

Let us first consider  $1/4 < \gamma < 4/15$ . If  $\eta_\perp(R^*) = 0$ , the system undergoes Berezinskii-Kosterlitz-Thouless transition and  $\pi \rho_K / 2T = 1$ , where  $N_1 - N_4$  vortices become relevant,  $\langle \cos 2\pi \theta \rangle \neq 0$ . At the same time,  $\langle \cos \pi \theta \rangle \neq 0$  and the remaining factor of the half-vortex operator becomes relevant, with the dimensionality  $\pi \rho_K / 4\gamma T$ . As a result, the U(1) sector also becomes disordered.

Initial steps in the consideration of  $\eta_\perp \neq 0$  are the same as in the derivation of Eqs. (4.30) and (4.31), and we obtain two lines of the Ising phase transitions. The scaling of the half-vortex fugacity on the Ising line is still governed by Eq. (4.50) so that the conclusions of Eqs. (4.51) and (4.53) remain intact [see Fig. 7(b)].

The peculiarity of the  $4/15 < \gamma < 1/3$  regime is that the half-vortex operator becomes relevant in the whole Ising line, whereas it is still irrelevant in the ordered region. As a result, the points  $D_{1,2}$  on Fig. 7(b) collapse [see Fig. 7(c)]. The positions of the Berezinskii-Kosterlitz-Thouless lines still can be estimated using Eqs. (4.51) and (4.52).

The most delicate case which we were not able to solve is  $\gamma > 1/3$ . In this situation, the half-vortices are always more relevant than the vortices and the transitions both in U(1) and in  $N_1 - N_4$  sectors occur due to the half-vortices. The corresponding free energy obtained by keeping only half-vortices in Eq. (4.48) is

$$\begin{aligned} \frac{\mathbb{F}_{14}}{T} = & \frac{\rho_K}{2T} (\partial_x \phi)^2 + \frac{T}{2\rho_K} (\partial_x \theta)^2 + i \partial_x \theta \partial_y \phi + \frac{\rho_K}{2\gamma T} (\partial_x \theta_s)^2 \\ & + \frac{T\gamma}{2\rho_K} (\partial_x h_s)^2 + i \partial_x h_s \partial_y \theta_s + \frac{\mu_{1/2}}{R_*^2} \cos(\pi h_s) \cos(\pi \theta) \\ & + \frac{\eta_\perp}{R_*^2 T} \cos 2\phi. \end{aligned} \quad (4.57)$$

We do not know the critical property of this model in the strong coupling limit.

## 2. Vicinity of lines $\eta_z > 0$ , $\eta_\perp = \pm \eta_z$

The analysis of those lines relies on the materials of Secs. IV C 1 and IV B 2. Near the line  $\eta_z > 0$ ,  $\Delta \eta = |\eta_\perp| - \eta_z \ll \eta_z$ , we have to generalize Eq. (4.37) [see also Eq. (4.38)] to include U(1) sector. In this section, we also neglect the hexadic anisotropy  $\zeta = 0$ . The resulting theory is obtained from Eq. (4.12) by putting an extra constraint on the unitary matrix  $\hat{V}$



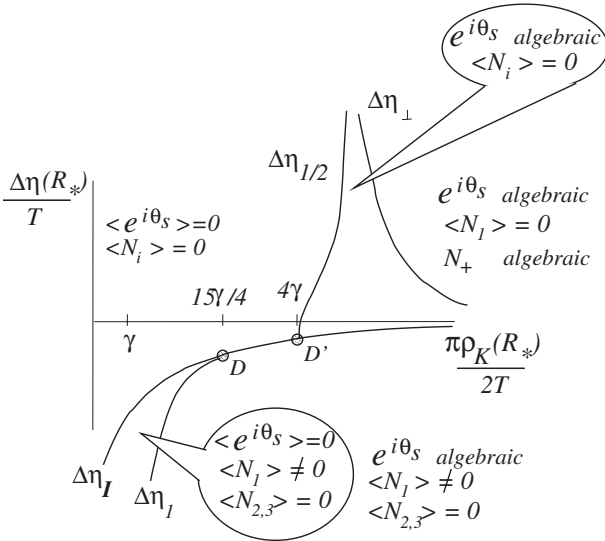


FIG. 8. Phase diagrams in the vicinity of the line  $\Delta\eta = \eta_z + \eta_\perp \ll \eta_z, \eta_z > 0$  for finite value of  $\gamma$  [see Eq. (4.47)] and in the absence of the hexadic anisotropies,  $\zeta = 0$ . Here,  $N_+ = N_2 + iN_3$ . Lines  $\Delta\eta_{\perp,1,1/2}$  are the Berezinskii-Kosterlitz-Thouless phase transitions. Line  $\eta_I$  is the Ising-type phase transition. The asymptotics of the lines  $\Delta\eta_{1,1/2}$  are given by Eqs. (4.53) and (4.56) for points  $D$  and  $D'$ , respectively [those points are equivalent to the multicritical points of Fig. 7(a) with the same notation]. The transitions across the lines  $\Delta\eta_{1,\perp}$  are controlled by the unbinding of the vortices, and  $\Delta\eta_{1/2}$  is governed by the half-vortices.

$$\hat{V}^\dagger = -\hat{V}, \quad \eta_\perp < 0,$$

$$\hat{V}^\dagger = \hat{\tau}_y \hat{V} \hat{\tau}_y, \quad \eta_\perp > 0. \quad (4.58)$$

One case is mapped to the other by the substitution  $\hat{V} \rightarrow i\hat{\tau}_y \hat{V}$ , and therefore, only one of them has to be studied. The line  $\Delta\eta_I$  [see Eq. (4.41)] is of the Ising type, and all the analyses of Eqs. (4.50)–(4.56) are still valid.

What remains is the vicinity of the Berezinskii-Kosterlitz-Thouless transition line  $\Delta\eta_\perp$  (see Fig. 8). The theory describing phase transition in this case [compare with Eq. (4.42)] can be written in terms of dual fields only,

$$\mathcal{Z} \propto \int \mathcal{D}h_s \mathcal{D}\theta \exp\left(-\frac{\mathbb{F}_{23}}{T}\right),$$

$$\begin{aligned} \frac{\mathbb{F}_{23}}{T} = & \frac{T}{2\rho_K(R_{**})} (\partial_\mu \theta)^2 + \frac{T}{2\rho_s} (\partial_\mu h_s)^2 \\ & + \frac{\mu_{23}(\Delta\eta)}{R_{**}^2} \cos 2\pi\theta + \frac{\mu_{1/2}(\Delta\eta)}{R_{**}^2} \cos \pi h_s \cos \pi\theta, \end{aligned} \quad (4.59)$$

where  $\rho_s \gg \rho_K(R_{**})$  because of the strong logarithmic renormalization at distances where the valley sector is almost isotropic. It has a sequence of two phase transitions shown in Fig. 8 by lines  $\Delta\eta_\perp$  and  $\Delta\eta_{1/2}$ .

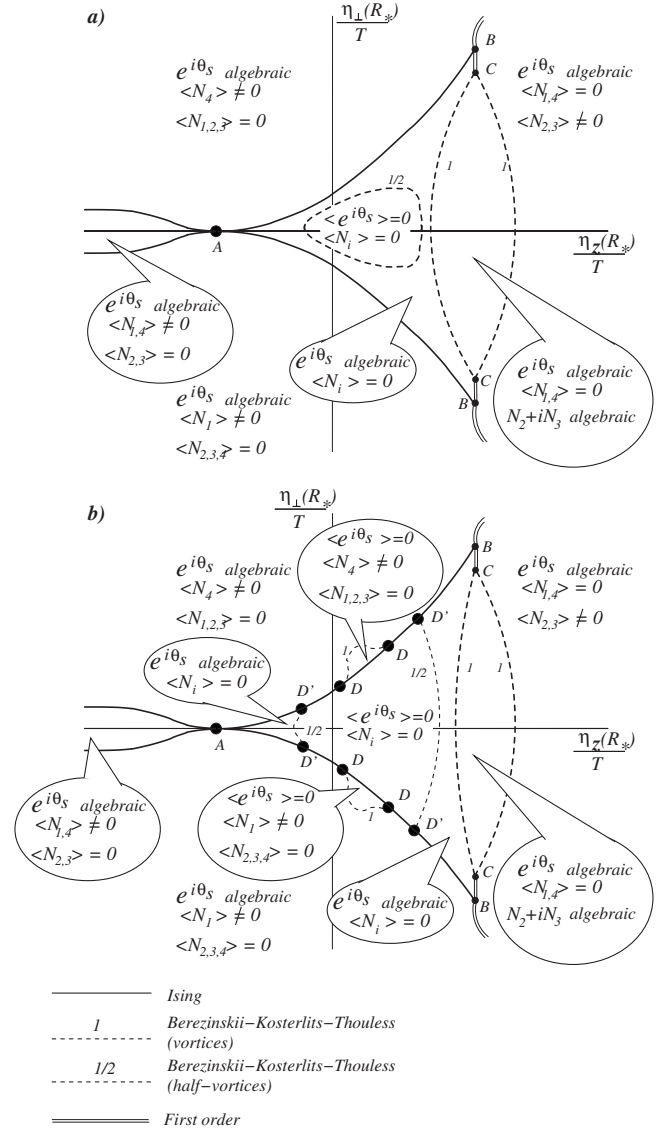


FIG. 9. The overall phase diagram for (a) decoupled valley and spin sectors,  $\gamma \rightarrow 0$ , and (b) for  $\gamma < 1/4$ . The positive quartic anisotropy,  $\kappa > 0$ , is assumed. The more detailed behavior near the multicritical points  $A$ ,  $B$ ,  $C$ , and  $D$  are shown in more detail in Figs. 5–8. The notation for those points here is consistent with that for Figs. 5–9.

#### D. Resulting phase diagram

In Secs. IV B and IV C, we analyzed the vicinities of the point degeneracies and the vicinities of the line degeneracies of Fig. 4. The results of this analysis enabled us to construct the phase diagrams in terms of the plane defined by anisotropies  $[\eta_z(R_*), \eta_\perp(R_*)]$  [see also Eqs. (4.21) and (4.22)]. Indeed, there can be no other singularities than those we have already considered, because for all the other regions of the phase diagrams, the  $SU(2)$  sector is massive due to the anisotropies. Therefore, the character of the singularities along the phase transition line remains the same.

Bearing this in mind and expressing  $\rho_K(R_*)$  in terms of anisotropies using Eq. (4.23), we construct the “global” phase diagram shown in Fig. 9. The relation of this phase

diagram to the physical coordinates  $B$ ,  $T$  will be found in Sec. V E after the microscopic theory for the parameters of Landau free energy is built.

## V. LOGARITHMIC RENORMALIZATIONS AND MEAN-FIELD TRANSITION

The specifics of the problem at hand is that it has three different intervals of the logarithmic renormalizations: (i) energies larger than the Zeeman splitting; (ii) energies larger than the temperature, but smaller than the Zeeman splitting; and (iii) classical renormalizations considered in the previous section. As those renormalizations are contributed by different degrees of freedoms, they have to be considered separately. The result will be the microscopic expressions for the coupling constants in the free energy, which will enable us to construct the physical phase diagram in Sec. V E.

### A. Logarithmic renormalizations at energies larger than the Zeeman splitting

At such energies, the Zeeman splitting is not important and can be considered perturbatively if necessary. We will also assume that the short-range interaction and umklapp terms are not strong enough to lead to any reconstruction in the state of the system at high energies, so they also can be considered within the perturbation theory, leading to a simple modification of the coupling constants which are not well known anyway.

The only terms which require special attention are those related to the long-range Coulomb interaction. Indeed, a simple dimensional analysis of the Hamiltonian (2.10) and (2.11) points to logarithmic divergences in the simple perturbation theory (first identified in Ref. 6 for the three-dimensional gapless semiconductors).

As usual, a summation of the leading logarithmic divergences is performed within the renormalization group scheme. However, the loop expansion would not be suitable for the description of the graphene as the dimensionless interaction strength  $e^2/v(r_c)$  is not small at distances  $r_c \approx a$ .

Instead, the expansion in terms of  $N$ —the number of independent fermion species entering the Hamiltonian (2.10) and (2.11)—will be used. For the problem at hand, we have the valley and spin degeneracies, so that  $N=4$ . The results, which will be obtained, indicate that  $1/N$  corrections are quite small for  $N=4$ , so that  $1/N$  expansion seems to be a reasonable approximation.

To make the calculations compact, we will utilize the standard imaginary time diagrammatic technique.<sup>16</sup> Analytic expressions for the corresponding lines are given in Fig. 10.

Performing the renormalization group procedure, we change the smallest spatial scale in the problem from  $r_c^<$  to the exponentially larger scale  $r_c^>$ . It amounts to taking into account all the diagrams where the momenta  $q$  going through the Coulomb interaction propagator belong to the region  $1/r_c^> < |q| < 1/r_c^<$ . This cutoff procedure does not violate the gauge invariance or other symmetries of the problem. Then, we rescale fermionic fields as  $\psi \rightarrow (1 + \delta Z/2)\psi$ ,  $\bar{\psi} \rightarrow (1 + \delta Z/2)\bar{\psi}$  in order to keep the term  $\bar{\psi}\partial_t\psi$  intact. [In this

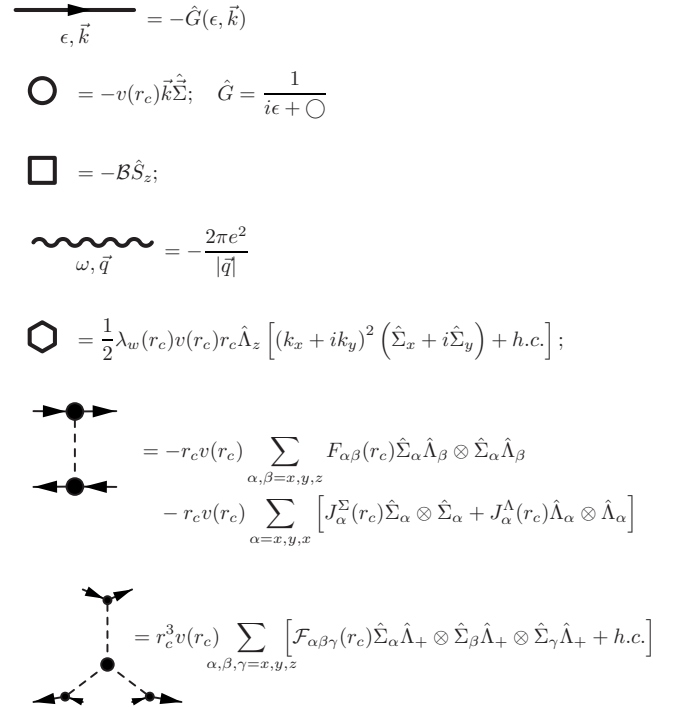


FIG. 10. Basic elements for the diagrammatic calculation for Hamiltonian (2.9)–(2.13), (2.14a), (2.14b), and (2.15)–(2.17), at distances  $r_c \lesssim R_B \equiv v(R_B)/B$ .

scheme, the scalar vertex and the Zeeman splitting term are not renormalized also, as a consequence of the gauge invariance. This can be checked by explicit calculation of the diagrams of Figs. 11(e) and 11(f).]

For the high-symmetry part of the Hamiltonian [see Eqs. (2.10) and (2.11)], the only coupling which renormalizes is the velocity  $v(r_c)$ . This renormalization is a consequence of the non-Lorentzian invariance of the Coulomb interaction.

Introducing the dimensionless interaction strength

$$g(r_c) = \frac{\pi e^2 N}{8v(r_c)}, \quad (5.1)$$

and calculating the diagrams of Fig. 11(d), we obtain

$$\frac{d \ln g}{d \ln r_c} = -\frac{8}{\pi^2 N} f_v(g), \quad (5.2)$$

where dimensionless function  $f_v$  is given by

$$f_v(g) = 1 - \frac{\pi}{2g} + \begin{cases} \frac{\arccos g}{g\sqrt{1-g^2}}, & g \leq 1 \\ \frac{\operatorname{arccosh} g}{g\sqrt{g^2-1}}, & g \geq 1. \end{cases} \quad (5.3a)$$

It is easy to see that the function  $f_v(g)$  is monotonously increasing and analytic for all  $g > 0$  (see Fig. 12). The asymptotic behavior of this function is

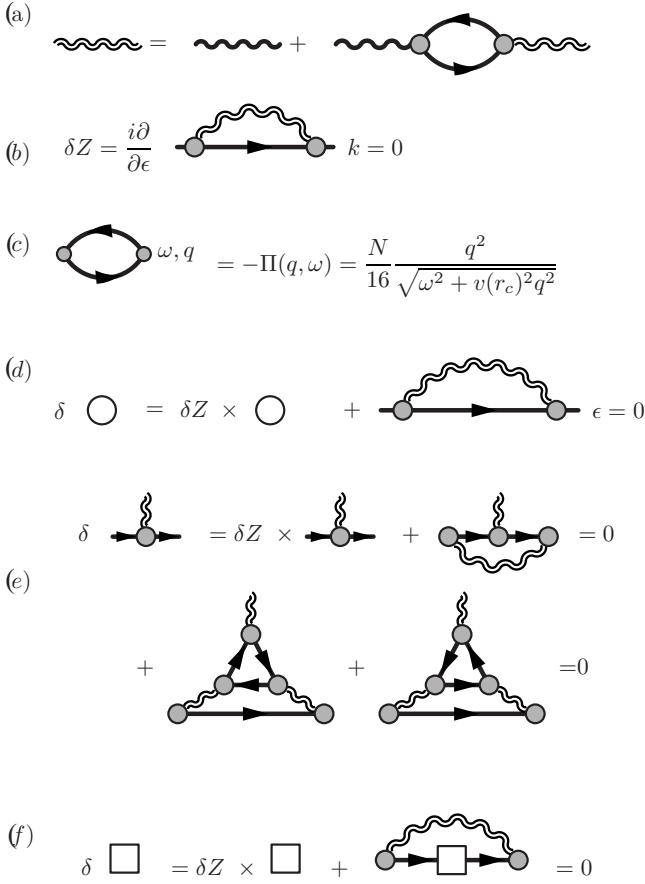


FIG. 11. Diagrammatic representation for the leading  $1/N$  renormalization of the parameters of the highly symmetric part of the Hamiltonian [see Eq. (2.10)]. All the basic elements are defined in Fig. 10. The integration over the momentum  $q$  going through the wiggly line is restricted by  $1/r_c^> < |q| < 1/r_c^<$ .

$$f_v(g) \approx \begin{cases} \frac{\pi g}{4} - \frac{2g^2}{3} + \mathcal{O}(g^3), & g \ll 1 \\ 1 - \frac{\pi}{2g} + \frac{\ln 2g}{g^2} + \mathcal{O}\left(\frac{1}{g^4}\right), & g \gg 1. \end{cases} \quad (5.3b)$$

Equations (5.2) and (5.3a) were first obtained in Ref. 7 for  $N=1$ , where they are not applicable beyond the first term in the expansion (5.3a) and (5.3b) for  $g \ll 1$ . The validity of those formulas for  $N \gg 1$  was pointed out in Ref. 8, but the numerical coefficients here are different from the latter reference.

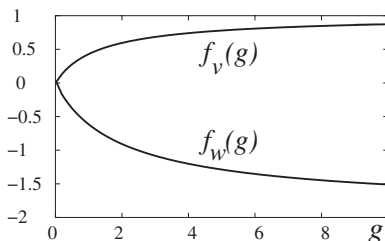


FIG. 12. Plots of functions  $f_v(g)$  and  $f_w(g)$  entering into renormalization group equations.

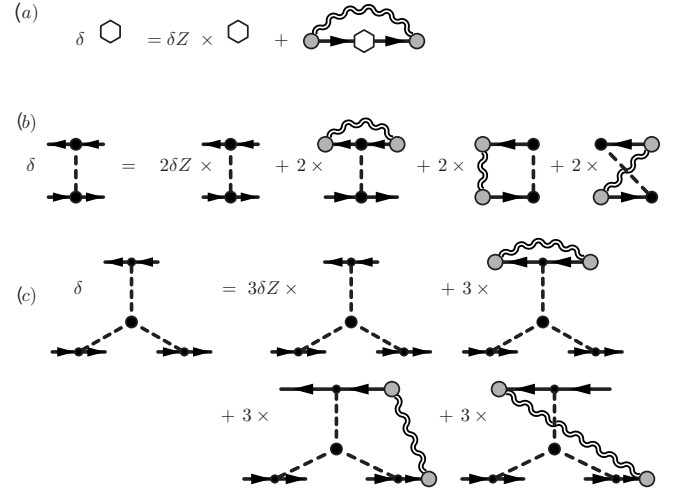


FIG. 13. Diagrammatic representation for the leading  $1/N$  renormalization of the parameters of the low-symmetry part of the Hamiltonian [see Eqs. (2.13), (2.14a), (2.14b), and (2.16)]. All the basic elements are defined in Figs. 10 and 11. The integration over the momentum  $q$  going through the wiggly line is restricted by  $1/r_c^> < |q| < 1/r_c^<$ .

Solution of Eq. (5.2) with the help of the asymptotics (5.3b) yields

$$g\left(\frac{r_c}{\mathcal{R}}\right) \approx \begin{cases} \left[ \frac{2}{N\pi} \ln\left(\frac{r_c}{\mathcal{R}}\right) + 1 \right]^{-1}, & r_c \geq \mathcal{R} \\ \left(\frac{\mathcal{R}}{r_c}\right)^{8/\pi^2 N} \approx \left(\frac{\mathcal{R}}{r_c}\right)^{0.20}, & a \ll r_c \leq \mathcal{R}, \end{cases} \quad (5.4)$$

where  $\mathcal{R}$  is the only relevant spatial scale generated by the interaction. This scale can be estimated as

$$\ln \frac{\mathcal{R}}{a} \approx \begin{cases} \frac{\pi^2 N}{8} \ln g(a), & g(a) \geq 1 \\ -\frac{\pi N}{2g(a)}, & g(a) \leq 1, \end{cases} \quad (5.5)$$

where  $a$  is the scale of the order of the lattice constant at which the continuous description becomes applicable.

For the graphene sheets, the reported velocity (see, e.g., Ref. 17) is  $v(a) \approx 10^8$  cm/s. We estimate  $g \approx 2-4$  (the uncertainty is associated with the dielectric properties of the substrate as well as the uncertainty of the linear scale at which the velocity is measured) and we find from Eq. (5.5)

$$\mathcal{R} \approx 10^2 - 10^3 a \gg a. \quad (5.6)$$

For all further considerations, we assume that the relation  $\mathcal{R} \gg a$  is fulfilled.

The Coulomb interaction strongly affects the scaling of the low-symmetry terms of the Hamiltonian. Let us start from the trigonal warping term (2.13). By calculating the diagrams shown in Fig. 13(a), we find

$$\frac{d \ln \lambda_w}{d \ln r_c} = -1 + \frac{4}{\pi^2 N} f_w(g), \quad (5.7)$$

where the negative monotonous analytic function

$$f_w(g) = -\frac{28}{15} + \frac{13\pi}{8g} + \frac{10}{g^2} - \frac{11\pi}{2g^3} - \frac{6}{g^4} + \frac{3\pi}{g^5} + \left(-\frac{4}{g} + \frac{7}{g^3} - \frac{3}{g^5}\right) \times \begin{cases} \frac{2 \arccos g}{\sqrt{1-g^2}}, & g \leq 1 \\ \frac{2 \operatorname{arccosh} g}{\sqrt{g^2-1}}, & g \geq 1 \end{cases} \quad (5.8a)$$

is also plotted in Fig. 12.

The asymptotic behavior of this function is

$$f_w \approx \begin{cases} -\frac{5\pi g}{16} + \frac{64g^2}{105} + \mathcal{O}(g^3), & g \ll 1 \\ -\frac{28}{15} + \frac{13\pi}{8g} + \frac{10-8\ln 2g}{g^2} + \mathcal{O}\left(\frac{1}{g^3}\right), & g \gg 1. \end{cases} \quad (5.8b)$$

Solution of Eq. (5.7) with the help of Eq. (5.8b) yields

$$\frac{\lambda_w(r_c)}{\lambda_w(\mathcal{R})} \approx \begin{cases} \left(\frac{\mathcal{R}}{r_c}\right) \left[ \frac{2}{N\pi} \ln\left(\frac{r_c}{\mathcal{R}}\right) + 1 \right]^{-5/8}, & r_c \geq \mathcal{R} \\ \left(\frac{\mathcal{R}}{r_c}\right)^{1+(112/5\pi^2 N)} \approx \left(\frac{\mathcal{R}}{r_c}\right)^{1.57}, & a \ll r_c \leq \mathcal{R}, \end{cases} \quad (5.9)$$

where

$$\lambda_w(\mathcal{R}) \approx \lambda_w(a) \left(\frac{a}{\mathcal{R}}\right)^{1.57} \approx 10^{-3} - 10^{-5}. \quad (5.10)$$

Thus, we see that the Coulomb interaction tends to suppress drastically the warping term, making the energy surfaces more and more isotropic.<sup>18</sup>

On the other hand, the Coulomb interaction leads to the enhancement of the short-range interaction terms in the Hamiltonian (2.14a) and (2.14b). Calculating the diagrams of Fig. 13(b), we find

$$\begin{aligned} \frac{d \ln F_+^{\Sigma,\perp}}{d \ln r_c} &= \frac{d \ln J_+^{\Sigma,\Lambda}}{d \ln r_c} = \frac{d \ln J_-^\Lambda}{d \ln r_c} = -1, \\ \frac{d \ln F_-^{\Sigma,\perp}}{d \ln r_c} &= \frac{d \ln J_-^\Sigma}{d \ln r_c} = -1 + \frac{40}{\pi^2 N} f_v(g), \end{aligned} \quad (5.11)$$

where function  $f_v(g)$  is defined in Eq. (5.3a). [Notice that the ‘‘mean-field analysis’’ of Ref. 5 of the excitonic instabilities at zero magnetic field corresponds to accounting for only the third diagram in the right-hand side of Fig. 13(b), and thus, is false even within  $1/N$  approximation.]

Equations (5.11) can be easily solved with the help of Eq. (5.2), and we find

$$\frac{F_+^{\Sigma,\perp}(r_c)}{F_+^{\Sigma,\perp}(a)} = \frac{J_+^{\Sigma,\Lambda}(r_c)}{J_+^{\Sigma,\Lambda}(a)} = \frac{J_-^\Lambda(r_c)}{J_-^\Lambda(a)} = \frac{a}{r_c}, \quad (5.12a)$$

$$\frac{F_-^{\Sigma,\perp}(r_c)}{F_-^{\Sigma,\perp}(a)} = \frac{J_-^\Sigma(r_c)}{J_-^\Sigma(a)} = \frac{a}{r_c} \left(\frac{g(a)}{g(r_c)}\right)^5. \quad (5.12b)$$

Couplings in the Eq. (5.12a) are irrelevant. The interactions in Eq. (5.12b) are strongly enhanced by the long-range Coulomb interaction. This enhancement becomes especially pronounced at intermediate distances  $r_c \lesssim \mathcal{R}$ . Using Eq. (5.4), we find

$$\frac{F_-^{\Sigma,\perp}(r_c)}{F_-^{\Sigma,\perp}(a)} = \frac{J_-^\Sigma(r_c)}{J_-^\Sigma(a)} \approx \left(\frac{r_c}{a}\right)^{(40/\pi^2 N)-1} \approx \left(\frac{r_c}{a}\right)^{0.01},$$

i.e., naively dimensionally irrelevant couplings become weakly relevant. Though, such small value of indices is clearly beyond the accuracy of the  $1/N$  approximation for  $N=4$ , this formula indicates, however, that the effect of the short-range interaction lowering the symmetry of the system is much stronger than it was thought before. Whether or not this enhancement may lead to instability at zero magnetic field requires further improvement of the renormalization group scheme, which is beyond the scope of the present paper. Here, we simply note that at large distances,  $g \rightarrow 1/\ln(r_c)$  [see Eq. (5.4)], so that the coupling of Eq. (5.12b) becomes irrelevant again. It indicates that at zero magnetic field, the excitonic instability can occur only as a first order phase transition. In all subsequent consideration, we will assume that such transition does not occur. This assumption is in accord with all the experimental findings accumulated so far.

For further use, let us recast the answers (5.12a) and (5.12b) for the most important constants, in the form similar to Eq. (5.9). Because of estimate (5.6), the second digits in the exponents are not observable and will be omitted:

$$F_-^{\Sigma,\perp}(r_c) \approx \begin{cases} F_-^{\Sigma,\perp}(\mathcal{R}), & r_c \leq \mathcal{R} \\ F_-^{\Sigma,\perp}(\mathcal{R}) \frac{\mathcal{R}}{r_c} \left[ \frac{2}{N\pi} \ln\left(\frac{r_c}{\mathcal{R}}\right) + 1 \right]^5, & r_c \geq \mathcal{R}, \end{cases} \quad (5.13)$$

$$F_-^{\Sigma,\perp}(\mathcal{R}) \approx F_-^{\Sigma,\perp}(a) \approx 1.$$

Finally, the umklapp terms are also enhanced by the interaction. Calculating the contributions shown in Fig. 13(b), we obtain the renormalization group equations

$$\begin{aligned} \frac{d \ln \mathcal{F}_+}{d \ln r_c} &= -3, \\ \frac{d \ln \mathcal{F}_-}{d \ln r_c} &= -3 + \frac{64}{\pi^2 N} f_v(g). \end{aligned} \quad (5.14)$$

Similar to Eqs. (5.12a) and (5.12b), the solution of Eq. (5.14) is

$$\frac{\mathcal{F}_+(r_c)}{\mathcal{F}_+(a)} = \left(\frac{a}{r_c}\right)^3, \quad \frac{\mathcal{F}_+(r_c)}{\mathcal{F}_+(a)} = \left(\frac{a}{r_c}\right)^3 \left(\frac{g(a)}{g(r_c)}\right)^8. \quad (5.15)$$

In particular, at the intermediate distances  $r_c \lesssim \mathcal{R}$ , we find

$$\frac{\mathcal{F}_+(r_c)}{\mathcal{F}_+(a)} \approx \left(\frac{a}{r_c}\right)^{3-(64/\pi^2 N)} \approx \left(\frac{a}{r_c}\right)^{1.4},$$

i.e., the three-particle umklapp interaction remains irrelevant though it is strongly enhanced by the Coulomb interaction.

To conclude this section, we notice that the short-range interaction terms are vital in the consideration of the quantum Hall effect ferromagnets,<sup>19,20</sup> and the effect of warping on the weak localization was considered in Ref. 21. The results of this section indicate that the estimates done in those works are hardly reliable.

### B. Logarithmic renormalizations at energies smaller than the Zeeman splitting: Separation of the electron-hole and Cooper channels

In the previous section, we considered the Zeeman splitting as a perturbation. This is legitimate up to the spatial scale  $r_c < R_B$ , where the length  $R_B$  is found from the equation

$$v\left(\frac{R_B}{\mathcal{R}}\right) = \mathcal{B}R_B. \quad (5.16)$$

The scale dependent velocity  $v$  is determined from Eqs. (5.1) and (5.2), and we highlighted that this dependence may include only one spatial scale  $\mathcal{R}$ . To solve Eq. (5.16) and facilitate further discussion, we introduce the natural scale for the Zeeman splitting,  $\mathcal{B}_0$ , according to

$$\mathcal{B}_0 = \frac{v(r_c = \mathcal{R})}{\mathcal{R}}, \quad (5.17)$$

rough estimate for  $\mathcal{B}_0$  is  $\mathcal{B}_0 \approx 10\text{--}10^2$  K. Then the solution of Eq. (5.16) takes the universal form

$$R_B = \mathcal{R}f_B\left(\frac{B}{B_0}\right), \quad (5.18)$$

where the function  $f_B(x)$  is the solution of the equation

$$\begin{aligned} v[f_B(x)] &= xv(1), \\ f_B(x) &\approx 1/x^{1.25}, \quad x \geq 1, \\ f_B(x) &\approx \frac{2}{N\pi x} \ln\left(\frac{1}{x}\right) + \frac{1}{x}, \quad x \leq 1. \end{aligned} \quad (5.19)$$

At  $r_c > R_B$ , Zeeman splitting freezes some electronic degrees of freedom and, on the other hand, gives rise to the finite density of states for the other ones [see Fig. 2(b)].

To make use of such separation, we will include the Zeeman splitting in the denominator of the Green function and decompose the result as

$$\begin{aligned} \hat{G} &= \frac{1}{i\epsilon - v(R_B)\vec{k}\hat{\Sigma} - \mathcal{B}\hat{S}_z} = \hat{G} + \delta\hat{G}, \\ \hat{G} &= \hat{P}(\vec{n})\frac{1}{i\epsilon - \xi\hat{S}_z}, \quad \delta\hat{G} = (1 - \hat{P}(\vec{n}))\frac{1}{i\epsilon + (\xi - 2\mathcal{B})\hat{S}_z}, \\ \xi &\equiv \mathcal{B} - v(R_B)|\vec{k}|, \quad \vec{n} = \frac{\vec{k}}{|\vec{k}|}, \end{aligned} \quad (5.20)$$

where

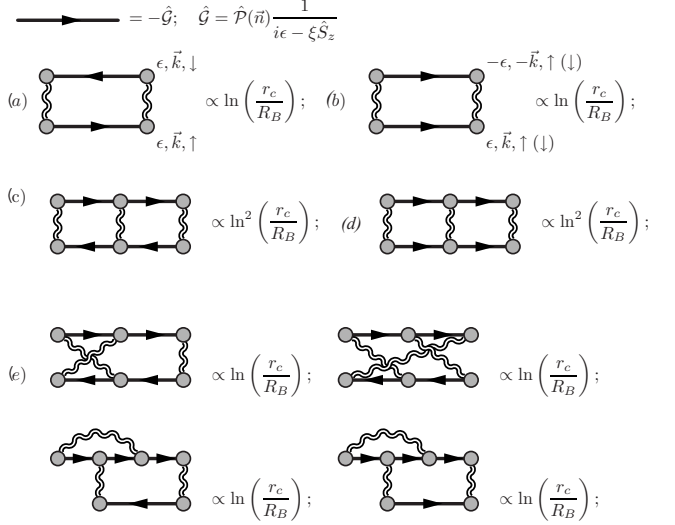


FIG. 14. [(a)–(d)] Leading and (e) subleading logarithmic divergences at  $r_c > R_B$ . Series (a) and (c) corresponds to the excitonic instability (Ref. 11) in the electron-hole channel studied in the present series. The interaction in the Cooper channel [(b) and (d)] is repulsive and, therefore, renormalizes to zero.

$$\hat{P} \equiv \frac{1}{2}(1 - \vec{n} \cdot \hat{\Sigma}\hat{S}_z), \quad \hat{P}^2 = \hat{P} \quad (5.21)$$

is the projection operator to the branches of the electron spectrum, which may produce excitations with the energies smaller than  $\mathcal{B}$ .

The  $\delta\mathcal{G}$  component of the Green function (5.20) does not have a resonant denominator and may be neglected. For the logarithmically divergent contributions, only  $\xi \lesssim \mathcal{B}$  are important, so that the integration over the momentum can be replaced by

$$\int \frac{d^2k}{(2\pi)^2} \dots \rightarrow \int \frac{d\vec{n}}{2\pi} \int_{-\mathcal{B}}^{\mathcal{B}} \frac{d\xi}{2\pi v^2(R_B)} \dots \quad (5.22)$$

Usual calculation of the second order correction to the interaction vertex shown on Figs. 14(a) and 14(b) reveals two logarithmically divergent contributions, which can be readily identified as (a) electron-hole and (b) Cooper channels. It is worthwhile to emphasize that those contributions are associated with the presence of the Fermi surface, and have a structure very different from the high-energy logarithmic terms of the previous section.

To collect the leading logarithmic divergences, we look at the third order diagram and find that only those corresponding to the ladder series [see Figs. 14(b) and 14(d)] are proportional to the second power of the logarithm. The subleading terms [see Fig. 14(e)] can be combined as a perturbative (in  $1/N$ , or the interaction strength) renormalization of the coefficients in the second order diagram and, therefore, can be neglected.

Finally, it is easy to check that the signs of the diagrams in Figs. 14(a) and 14(c) are the same, whereas the signs of the diagrams in Figs. 14(b) and 14(d) are different from each other. The latter corresponds to the repulsive interaction in





$$\Delta_0(T=0) \approx 2\mathcal{B} \exp\left(-\frac{\pi \left[ \ln \frac{\mathcal{B}_0}{\mathcal{B}} + \frac{N\pi}{2} \right]}{4 \ln \left[ \ln \frac{\mathcal{B}_0}{\mathcal{B}} + \frac{N\pi}{2} \right]}\right). \quad (5.29a)$$

For the strong magnetic field,  $\mathcal{B} \gg \mathcal{B}_0$ , the result reads

$$\Delta_0(T=0) \approx 2\mathcal{B} \exp\left\{-2N \left[ 1 + \frac{1}{3} \left( \frac{\mathcal{B}_0}{\mathcal{B}} \right)^{8/\pi^2 N} \right]\right\}, \quad (5.29b)$$

i.e., the dependence slowly approaches the linear function.

To complete this section, we consider the effect of finite temperature. As for the usual BCS mean field, Eq. (5.23) gives the temperature dependence of the width of the mean-field gap  $\Delta_0(T)$ , which contains the scale  $\Delta_0(0)$  only:

$$\ln \frac{T_{MF}}{T} + \sum_{n=0}^{\infty} \left\{ \frac{1}{\sqrt{[n+(1/2)]^2 + [\Delta_0(T)^2/4\pi^2 T^2]}} - \frac{1}{n+(1/2)} \right\} = 0, \quad (5.30)$$

where  $T_c$  is related to  $\Delta_0(0)$  by the usual weak coupling BCS relation

$$T_{MF} = \pi e^{-C} \Delta_0(0) \approx 1.76 \Delta_0(0) \quad (5.31)$$

and  $C$  is the Euler constant.

Equations (5.31) and (5.30) enable us to estimate the upper bound for the mean-field crossover temperature. For  $N=4$ , we find

$$T_{MF} \lesssim 10^{-3} \mathcal{B}, \quad (5.32)$$

where  $\mathcal{B}$  is the Zeeman splitting. As the electron  $g$  factor in graphene is equal to 2, we estimate for the parallel magnetic field  $B \approx 40$  T,  $T_{MF} \approx 60$  mK, which does not seem to be nonrealistic. The other experimental realization could be putting the appropriate insulating ferromagnet on the top of the graphene film, so that the Zeeman splitting is caused by the corresponding exchange fields. The effective Zeeman splitting in this case may reach thousands of Kelvin.<sup>23</sup>

In the vicinity of the mean-field crossover  $T_c - T \ll T_c$ , we obtain from Eq. (5.30)

$$\Delta_0(T)^2 = \frac{8\pi^2}{7\zeta(3)} T_c (T - T_c) \approx 9.38 T_{MF} (T - T_{MF}), \quad (5.33)$$

and  $\zeta(x)$  is the Riemann  $\zeta$  function.

#### D. Microscopic calculation of the coefficients in the free energy and effective action

Using the symmetry arguments of Sec. III or by explicit calculation, one finds that the solution of the form (5.25) is not unique and, in fact, any order parameter of the form

$$\hat{\Delta}(\vec{n}) = \hat{\sigma}_z^{AB} \otimes \hat{Q} \{ \Delta_0(T) \hat{P}(\vec{n}) + \Delta_1(T) [1 - \hat{P}(\vec{n})] \} \quad (5.34)$$

solves Eq. (5.23), i.e., the fluctuation effects, studied in Sec. IV, are important. Here,  $4 \times 4$  matrix  $\hat{Q}$  is given by Eqs. (3.2a), (3.2b), (3.2c), (3.2d), and (3.2e).

The free energy and the effective action describe the contribution of configurations of the order parameter slowly varying in time and space. The time and space gradient terms describe the cost of creating an inhomogeneous configuration, whereas the anisotropy leads certain modes to become massive. To calculate the latter ones, it is sufficient to consider the homogeneous and time independent configurations of the order parameter  $\hat{Q}$  [see Eqs. (3.2a), (3.2b), (3.2c), (3.2d), and (3.2e), whereas to find the former, one has to expand in small gradients of  $\hat{Q}$ . [In principle, one can perform the gauge transformation  $\hat{Q} \rightarrow \hat{U} \hat{Q} \hat{U}^\dagger = \hat{S}_x$ , and expand the fermionic determinant in terms of the non-Abelian scalar,  $\hat{U}^\dagger \partial_\tau \hat{U}$ , and vector,  $\hat{U}^\dagger \partial_\mu \hat{U}$ , potentials. We have chosen not to do it here to avoid careful considerations of the terms arising from the non-gauge-invariant integration cutoff in Eq. (5.22)].

#### 1. Stiffness

To find the gradient terms, we expand the order parameter as

$$Q(\mathbf{r}) = \hat{Q} \left[ 1 - \frac{1}{2} \delta \hat{Q}^2(\mathbf{r}) \right] + \delta \hat{Q}(\mathbf{r}),$$

$$\delta \hat{Q}(\mathbf{r}) = \int \frac{d^2 k}{(2\pi)^2} e^{i\vec{k}\vec{r}} \delta \hat{Q}_{\mathbf{k}}. \quad (5.35)$$

In order to preserve the constraints (3.2b) up to the second order perturbation theory in  $\delta \hat{Q}$ , we require

$$\hat{Q} = \hat{Q}^\dagger, \quad \hat{Q} \delta \hat{Q} + \delta \hat{Q} \hat{Q} = 0,$$

$$(\mathbb{1}^{KK'} \otimes \hat{\tau}_z^y) \delta \hat{Q} (\mathbb{1}^{KK'} \otimes \hat{\tau}_z^y) = -\delta \hat{Q}. \quad (5.36)$$

Calculating the diagram in Fig. 16, we obtain for the isotropic part of the free energy

$$\begin{aligned} \mathbb{F}_\circ &= \frac{1}{2} \int \frac{d^2 q}{(2\pi)^2} T \sum_{\epsilon_m} \int \frac{d^2 k}{(2\pi)^2} [\text{Tr} \hat{G}_Q(\epsilon_m, \vec{k} + \vec{q}) \\ &\times \delta \hat{Q}_q \hat{G}_Q(\epsilon_m, \vec{k}) \delta \hat{Q}_{-q} \\ &- \text{Tr} \hat{G}_Q(\epsilon_m, \vec{k}) \delta \hat{Q}_q \hat{G}_Q(\epsilon_m, \vec{k}) \delta \hat{Q}_{-q}], \end{aligned} \quad (5.37)$$

where  $\epsilon_m$  are the fermionic Matsubara frequencies. The term in the last line is local and it comes from the interaction part of the Hamiltonian. Its explicit calculation is not necessary because  $\delta Q_{\omega=0, k=0}$  corresponds to the motion along the degenerate manifold which cannot produce any contribution to the free energy—this requirement fixes the term unambiguously.

Expanding the Green functions in powers of small momentum  $q$ , we find

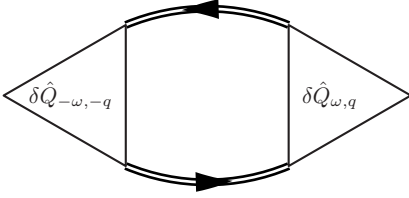
$$\begin{aligned} \overline{\overline{\epsilon_n, \vec{k}}} &= -\mathcal{G}_Q(\epsilon_n, \vec{k}); \\ \mathcal{G}_Q(\epsilon_n, \vec{k}) &= \hat{P}(\vec{n}) \frac{-i\epsilon_n - \xi \hat{S}_z - \hat{Q} \otimes \hat{\sigma}_z^{AB} \Delta_0}{\epsilon_n^2 + \xi^2 + \Delta_0^2} \\ S_o &= -\frac{1}{2} \left[ \delta \hat{Q}_{-\omega, -q} \quad \delta \hat{Q}_{\omega, q} \right] \end{aligned}$$


FIG. 16. Microscopic calculation of the stiffness and the collective mode velocity  $v_*$  in the effective action. Notation is defined in Eqs. (5.20) and (5.21).

$$\begin{aligned} \mathbb{F}_\circ &= -\frac{1}{4} \int \frac{d^2 q}{(2\pi)^2} T \sum_{\epsilon_m} \int \frac{d^2 k}{(2\pi)^2} \\ &\times \left[ q^2 \sum_{\mu=x,y} \text{Tr} \partial_k \hat{G}_Q(\epsilon_m, \vec{k}) \delta \hat{Q}_q \partial_k \hat{G}_Q(\epsilon_m, \vec{k}) \delta \hat{Q}_{-q} \right]. \end{aligned}$$

Then, the simple power counting shows that the integral is contributed by  $\epsilon$ ,  $vk \ll \mathcal{B}$ , and therefore, the integration rule (5.22) may be used. Finally, using the explicit expression for the Green function from Fig. 16 and Eq. (5.36), we obtain after simple algebra

$$\begin{aligned} \mathbb{F}_\circ &= \frac{\rho_K(T)}{8} \text{Tr} \int d^2 r (\nabla \hat{Q})^2, \\ \rho_K(T) &= \frac{\mathcal{B}}{4\pi} f_\rho \left( \frac{\Delta_0}{2\pi T} \right), \end{aligned} \quad (5.38)$$

where

$$\begin{aligned} f(x) &= \sum_{n=0}^{\infty} \frac{x^2}{[(n+1/2)^2 + x^2]^{3/2}} \\ &\approx \begin{cases} 1 - \pi x e^{-2\pi x} + \mathcal{O}(e^{-4\pi x}), & x \gg 1 \\ 7\zeta(3)x^2 - \frac{93\zeta(5)}{2}x^4 + \mathcal{O}(x^6), & x \ll 1, \end{cases} \end{aligned} \quad (5.39)$$

and  $\zeta(x)$  is the Riemann  $\zeta$  function.

At low temperatures,  $\Delta(T) \gg T$ , we find

$$\rho_K = \frac{\mathcal{B}}{4\pi} \quad (5.40)$$

independent of any logarithmic renormalization from higher energies.

In the opposite case,  $\Delta(T) \ll T$ , only constant in time fluctuations are important and we obtain  $S_o = \mathbb{F}_o/T$ , where  $\mathbb{F}_o$  is given by Eq. (4.4a) and the stiffnesses on the mean-field correlation length,  $\xi_{MF}$  [see Eq. (4.3)], are given by

$$\odot = \frac{\lambda_w(R_B)\mathcal{B}}{2} \hat{\Lambda}_z [(n_x + in_y)^2 (\hat{S}_x + i\hat{S}_y) + h.c.];$$

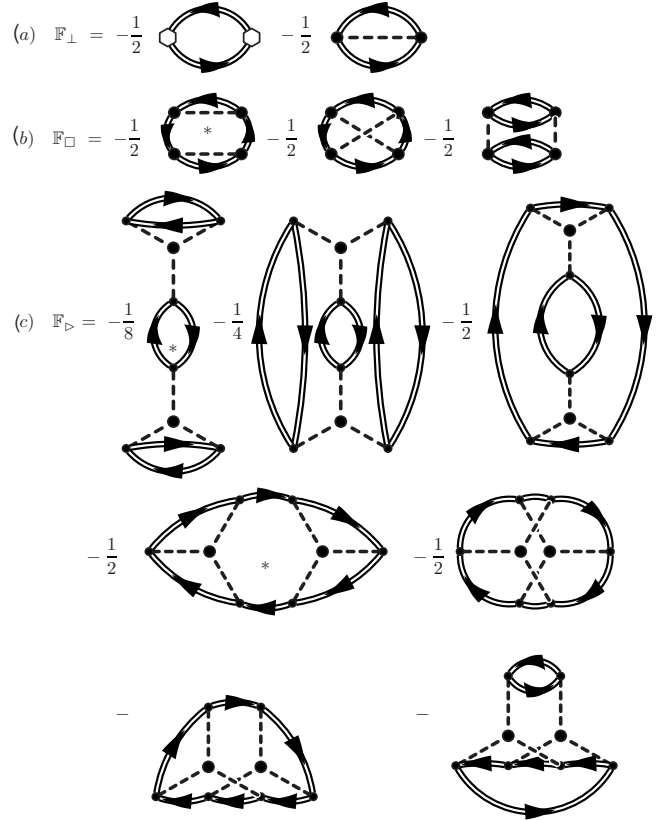
$$\begin{aligned} (a) \quad \mathbb{F}_\perp &= -\frac{1}{2} \left[ \text{Diagram 1} \right] - \frac{1}{2} \left[ \text{Diagram 2} \right] \\ (b) \quad \mathbb{F}_\square &= -\frac{1}{2} \left[ \text{Diagram 3} \right] - \frac{1}{2} \left[ \text{Diagram 4} \right] - \frac{1}{2} \left[ \text{Diagram 5} \right] \\ (c) \quad \mathbb{F}_\triangleright &= -\frac{1}{8} \left[ \text{Diagram 6} \right] - \frac{1}{4} \left[ \text{Diagram 7} \right] - \frac{1}{2} \left[ \text{Diagram 8} \right] \\ &\quad - \frac{1}{2} \left[ \text{Diagram 9} \right] - \frac{1}{2} \left[ \text{Diagram 10} \right] \\ &\quad - \left[ \text{Diagram 11} \right] - \left[ \text{Diagram 12} \right] \end{aligned}$$


FIG. 17. Microscopic calculation of the anisotropic terms in the free energy. Diagrams containing the largest power of  $\ln(\mathcal{B}/\Delta_0)$  are marked by a star.

$$\rho_K(\xi_{MF}) = \rho_s(\xi_{MF}) = \frac{\mathcal{B}}{2\pi} \left( \frac{T_{MF} - T}{T_{MF}} \right), \quad (5.41)$$

where we used Eq. (5.33).

## 2. Leading anisotropies

The quadratic anisotropies (4.4c) arise both due to the warping of the single electron spectrum (2.13) and the short-range interactions (2.14a) and (2.14b). The diagrammatic calculation of these anisotropies is straightforward and it is shown in Fig. 17(a).

We find  $\mathbb{F}_\perp = \mathbb{F}_\perp^{(1)} + \mathbb{F}_\perp^{(2)}$ , where the first contribution is due to the warping

$$\mathbb{F}_\perp^{(1)} = -\text{Tr} \hat{Q} \hat{\Lambda}_z \hat{Q} \hat{\Lambda}_z \frac{\lambda_w^2(R_B)\mathcal{B}^3}{16\pi v^2(R_B)} f_\rho \left( \frac{\Delta_0}{2\pi T} \right), \quad (5.42a)$$

where  $f_\rho$  is given by Eq. (5.39).

The second diagram of Fig. 17(b) describes the effect of the short-range interaction (2.14a) and (2.14b). We take into account only the most relevant terms as specified in Eq. (5.12b). The term proportional to  $J_-^\Sigma$  does not contain the intervalley  $\Lambda$  matrices and, thus, does not cause the anisotropy. We find

$$\mathbb{F}_{\perp}^{(2)} = - \left[ F_{-}^z(R_B) \text{Tr}(\hat{Q}\hat{\Lambda}_z)^2 + F_{-}^{\perp}(R_B) \sum_{\mu=x,y} \text{Tr}(\hat{Q}\hat{\Lambda}_{\mu})^2 \right] R_B \nu(R_B) \times \left[ T \sum_n \int \frac{\mathcal{B} d\xi}{2\pi \nu^2(R_B)} \frac{\Delta_0(T)}{\epsilon_n^2 + \xi^2 + \Delta_0(T)^2} \right]^2. \quad (5.42b)$$

The logarithmic integral in Eq. (5.42b) is eliminated using Eq. (5.26), and we obtain Eq. (4.4c) at the scale  $r_0 = \xi_{MF}$  [see Eq. (4.3)] with the couplings

$$\eta_z = -\mathcal{B} \left\{ \frac{\lambda_w^2(R_B) \mathcal{B}^2}{2\pi \Delta_0(0)^2} \left[ \frac{\Delta_0^2(0)}{\Delta_0^2(T)} f_{\rho} \left( \frac{\Delta_0(T)}{2\pi T} \right) \right] + 2F_{-}^z(R_B) \times \left( \frac{2N}{\pi f_{\Delta} \left( \frac{\pi}{4g(R_B)} \right)} \right)^2 \right\}, \quad (5.43a)$$

$$\eta_{\perp} = -2\mathcal{B} F_{-}^{\perp}(R_B) \left( \frac{2N}{\pi f_{\Delta} \left( \frac{\pi}{4g(R_B)} \right)} \right)^2, \quad (5.43b)$$

where  $f_{\Delta}(x)$  is defined in Eq. (5.28a).

Equations (5.43a) and (5.43b) give complete expressions for the anisotropies in the free energy (4.4c) in terms of the microscopic coupling constants defined on the scale  $R_B$ . Equations (5.9), (5.12), (5.13), (5.4), (5.18), (5.19), (5.28a), (5.29a), and (5.29b) enable us to find the magnetic field dependence of the anisotropy constants. In the case of the strong magnetic field  $\mathcal{B} \gtrsim \mathcal{B}_0$  [see Eq. (5.17)], it yields

$$\eta_z \approx -\mathcal{B} \left\{ \lambda_w^2(\mathcal{R}) \left( \frac{68\mathcal{B}}{\mathcal{B}_0} \right)^{3.9} \left[ \frac{\Delta_0^2(0)}{\Delta_0^2(T)} f_{\rho} \left( \frac{\Delta_0(T)}{2\pi T} \right) \right] + 12.9 F_{-}^z(\mathcal{R}) \right\}, \quad (5.44a)$$

$$\eta_{\perp} \approx -12.9 \mathcal{B} F_{-}^{\perp}(\mathcal{R}).$$

For the weak magnetic field,  $\mathcal{B} \lesssim \mathcal{B}_0$ , we find

$$\eta_z \approx -\mathcal{B} \left\{ \lambda_w^2(\mathcal{R}) \left( \frac{\mathcal{B}}{5.1\mathcal{B}_0} \right)^2 \exp \left( \frac{\pi \left[ \ln \frac{\mathcal{B}_0}{\mathcal{B}} + 6.28 \right]}{2 \ln \left[ \ln \frac{\mathcal{B}_0}{\mathcal{B}} + 6.28 \right]} \right) \times \left[ \frac{\Delta_0^2(0)}{\Delta_0^2(T)} f_{\rho} \left( \frac{\Delta_0(T)}{2\pi T} \right) \right] \left[ 0.15 \ln \left( \frac{\mathcal{B}_0}{\mathcal{B}} \right) + 1 \right]^{-13/4} + 12.9 F_{-}^z(\mathcal{R}) \left( \frac{\mathcal{B}}{\mathcal{B}_0} \right) \left[ 0.15 \ln \left( \frac{\mathcal{B}_0}{\mathcal{B}} \right) + 1 \right]^4 \right\},$$

$$\eta_{\perp} \approx -12.9 \mathcal{B} F_{-}^{\perp}(\mathcal{R}) \left( \frac{\mathcal{B}}{\mathcal{B}_0} \right) \left[ 0.15 \ln \left( \frac{\mathcal{B}_0}{\mathcal{B}} \right) + 1 \right]^4. \quad (5.44b)$$

Comparison of the anisotropies from Eqs. (5.44a) and (5.44b) with the expressions for stiffness (5.41) together with the estimates  $F_{-}^z(\mathcal{R}) \approx 1$  indicates that the weak anisotropy case is possible only for  $\mathcal{B} \ll \mathcal{B}_0$ , and at the strong magnetic field, the anisotropy is dominating already at the mean-field correlation length (see Sec. IV C).

The very peculiar situation arises if  $F_{-}^z(\mathcal{R}) < 0$ , as we explained before; the value and the sign of this constant are determined by the details at the distances of the order of the lattice constant. In this case, the exchange and the warping produce the contribution of the different signs, and intersection of the Heisenberg line,  $\eta_z > 0$ ,  $|\eta_{\perp}| = |\eta_z|$  (see Sec. IV B 2) becomes possible. Using Eq. (5.44a) and estimates (5.10) and (5.13), we find the estimate for such field  $\mathcal{B}_H$

$$\mathcal{B}_H \approx 10^{-2} \mathcal{B}_0 \left( \frac{|F_{-}^z(\mathcal{R}) + |F_{-}^{\perp}(\mathcal{R})||}{\lambda_w^2(\mathcal{R})} \right)^{0.26} \approx 1 - 10 \mathcal{B}_0 \gtrsim \mathcal{B}_0. \quad (5.45)$$

The manifestation of this line on the phase diagram will be considered in Sec. V E.

Calculation of the other anisotropies is self-explanatory from diagrams in Figs. 17(b) and 17(c). Though, formally, they are of the same order in perturbation theory, they still can be classified in powers of  $\ln(\mathcal{B}/\Delta) \ll 1$ . Taking into account only the leading logarithmic contributions, and re-expressing the logarithmic expression using the mean-field equation (5.26), we find for anisotropy coefficients in Eqs. (4.4d) and (4.4e)

$$\kappa(\xi_{MF}) = \frac{\mathcal{B}}{2\pi} \left( \frac{N[F_{-}^z(\mathcal{R}) - 3J_{\perp}^{\Lambda}(\mathcal{R})]}{\pi f_{\Delta} \left( \frac{\pi}{4g(R_B)} \right)} \right)^2 f_{\rho} \left( \frac{\Delta_0(T)}{2\pi T} \right), \quad (5.46a)$$

$$\zeta(\xi_{MF}) = \frac{2\mathcal{B}}{\pi} [F_{-}^z(\mathcal{R})]^2 D \left[ \frac{N}{\pi f_{\Delta} \left( \frac{\pi}{4g(R_B)} \right)} \right] \times \left( \frac{\Delta_0(T)}{\Delta_0(0)} \right)^2 f_{\rho} \left( \frac{\Delta_0(T)}{2\pi T} \right), \quad (5.46b)$$

where  $D(x) = xe^{-x}$ , and the functions  $f_{\rho, \Delta}$  are defined in Eqs. (5.39), (5.28a), and (5.28b). Deriving Eq. (5.46a), we took into account that  $\kappa$  is important only if  $\eta_{\perp} \rightarrow 0$  (see Sec. IV B 1). Thus, the irrelevant constants [see Eqs. (5.12a)] had to be taken into account.

Expressions (5.46a) and (5.46b) together with Eqs. (5.12a) and (5.15) show that those anisotropies are very small, so we will not analyze their asymptotics further.

### E. Phase diagram in $\mathcal{B}$ - $T$ plane

This section combines the symmetry analysis of Sec. IV with the microscopic calculation of the free energy couplings in Sec. V D. As a result, we will construct the phase diagram in the plane determined by the Zeeman splitting  $\mathcal{B}$  and by the system temperature  $T$ . As we have discussed in Sec. IV, the

interesting phase transitions are determined by the thermal fluctuations, and it is convenient to introduce the dimensionless Ginzburg-Levanyuk parameter

$$Gi \equiv \frac{4T_{MF}}{B} \ll 1, \quad (5.47)$$

characterizing the strength of such fluctuations. Here, the mean-field transition temperature is given by Eqs. (5.31), (5.27), (5.28a), (5.28b), (5.29a), and (5.29b).

Apparently, not all the regions of the phase diagram of Fig. 9 can be explored by varying  $B$  and  $T$ , and we will restrict ourselves with two most realistic, as we believe, cases. Namely, we assume that the absolute values of the interaction constants  $|F_{\pm}^{\pm}(a)| \approx 1$ . For the sake of concreteness, we assume  $F_{-}^{\pm}(a) > 0$ . [The case of  $F_{-}^{\pm}(a) < 0$  is obtained by the replacement  $N_1 \leftrightarrow N_4$ .]

Let us consider, first, the case of  $F_{-}^{\pm} < 0$ . Then, according to Eqs. (5.43a) and (5.43b), one finds  $\eta_{z,\perp} < 0$ . The mean-field diagram obtained from Fig. 4 is trivial and includes the continuous transition from the disordered normal state to the spin-flux state [Fig. 3(d)] of the excitonic insulator (see Fig. 18).

The fine structure of the phase diagram [Fig. 18(b)] is obtained from the general Fig. 9 by using the microscopic expression for the free energy couplings derived in Sec. V D. The topological structure of the phase diagram is most easily obtained by the mapping of the paths in  $B, T$  plane to the path in the  $(\eta_z, \eta_{\perp})$  plane, as shown in Fig. 18(c).

The positions of the transitions lines on the phase diagrams are obtained by combining the phenomenological results of Sec. IV and the microscopic analysis of Sec. V D. For instance, using Eqs. (4.15) and (5.41), we obtain in the limit of the small vortex fugacity

$$\frac{T_{MF} - T}{T_{MF}Gi} \approx \begin{cases} 4 & \text{line (i)} \\ 1 & \text{line (ii)}. \end{cases} \quad (5.48a)$$

Analogously, using Eqs. (4.20), (4.14), and (5.44b), we obtain the position of the Ising line. With logarithmic accuracy, we find for line (iii) of Fig. 18(b)

$$\frac{T_{MF} - T}{T_{MF}Gi} \approx \begin{cases} \frac{1}{4} \ln \frac{B_0Gi}{B}, & B_0 \exp\left(-\frac{1}{Gi}\right) \lesssim B \ll B_0Gi \\ \rightarrow 0, & B \gtrsim B_0Gi. \end{cases} \quad (5.48b)$$

The case of  $F_{-}^{\pm} < 0$  is more sophisticated. As we noticed in Sec. V D, coefficient  $\eta_z$  changes its sign as a function of the magnetic field and, at some point, crosses the Heisenberg line at field  $B_H$ . At the mean-field level, it corresponds to the continuous transition between two kinds of excitonic insulator: spin-flux state [see Fig. 3(d)] and the link centered spin-density wave [see Figs. 3(b) and 3(c)].

Similar to the previous case, the fine structure of the phase diagram [Fig. 19(b)] is obtained from the general Fig. 9 by the mapping of the paths in  $B, T$  plane to the path in the  $(\eta_z, \eta_{\perp})$  plane, as shown in Fig. 19(c).

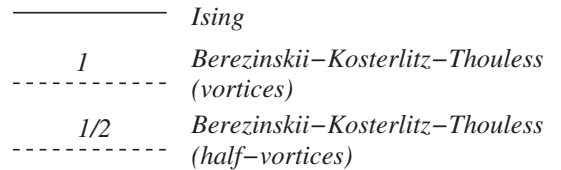
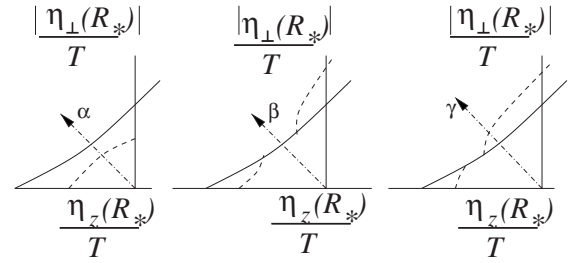
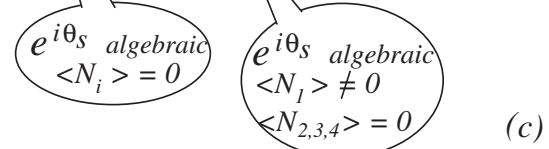
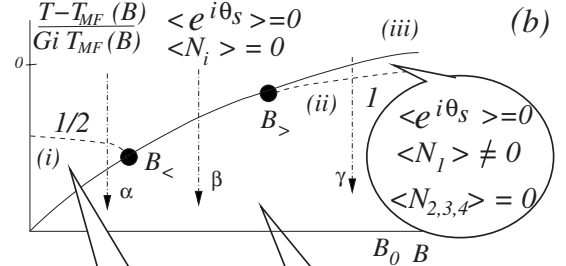
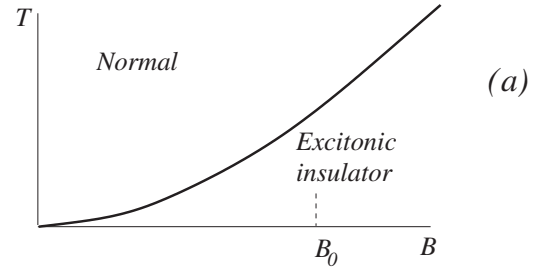


FIG. 18. Phase diagram of graphene in a parallel magnetic field for the short-range interaction constant  $F_{-}^{\pm} > 0$ . (a) Mean-field structure of the phase diagram. (b) The “fine” structure of the phase diagram in the close vicinity of the mean-field transition temperature,  $T_{MF}(B)$ . (c) Relation of the phase diagram (b) to the more phenomenological phase diagram of Fig. 9.

The Berezinskii-Kosterlitz-Thouless transition lines (i) and (ii) in Fig. 19(b) are still determined by the expressions (5.48a). Ising line (iv) and the Berezinskii-Kosterlitz-Thouless line are found from Eqs. (4.40a), (4.40b), and (5.41). Expanding

$$\Delta\eta \approx \left( \frac{B - B_H}{B_H} \right) \eta_{\perp},$$

we obtain with logarithmic accuracy for  $B_H \exp(-Gi) \ll B - B_H \ll B_H$ :



$$\frac{T_{MF}-T}{T_{MF}Gi} \approx \begin{cases} \frac{1}{8} \ln \frac{\mathcal{B}_H}{\mathcal{B}-\mathcal{B}_H} & \text{line (iv)} \\ \frac{1}{8} \ln \frac{\mathcal{B}_H}{\mathcal{B}_H-\mathcal{B}} & \text{line (v)}. \end{cases} \quad (5.49a)$$

For larger  $\mathcal{B}$ , the Ising line (iv) approaches the mean-field temperature. The Berezinskii-Kosterlitz-Thouless transition line (v) for  $\mathcal{B} \ll \mathcal{B}_H$  can be found using Eqs. (4.20), (4.14), and (5.44b). For the fields  $\mathcal{B}_0 \exp(-1/Gi) \leq \mathcal{B} \ll \mathcal{B}_0 Gi$ , this yields

$$\frac{T_{MF}-T}{T_{MF}Gi} \approx \frac{1}{4} \ln \frac{\mathcal{B}_0 Gi}{\mathcal{B}} \quad \text{line (v)}. \quad (5.49b)$$

The Berezinskii-Kosterlitz-Thouless line (vi) turns out to lie outside the fluctuation region due to the large numerical factor in Eq. (4.44) and the smallness of  $\zeta$  in Eq. (5.46b). We will not write down its asymptotic behavior.

This completes our analysis of the structure of the phase diagram of graphene in the parallel magnetic field characterized by the Zeeman splitting  $\mathcal{B}$ .

## VI. SUMMARY AND CONCLUSIONS

In this paper, we have discussed two problems concerning clean graphene: (i) possible effects of in-plane magnetic field in facilitating the formation of excitonic condensate and (ii) the role of the long-range Coulomb interaction and its influence on other interactions in the system. The second topic is more general than the first, and has a broader significance, though, as far as the paper is concerned; it was discussed in the second part.

In zero magnetic field, graphene is a gapless semiconductor with two Fermi points in the Brillouin zone (valleys). In-plane magnetic field pushes up- and down-spin bands in opposite directions, transforming the system into a metal with extended Fermi surfaces for electrons and holes of opposite spins. There are two such Fermi surfaces, corresponding to two possible valley indices. Electrons and holes attract through the Coulomb interaction, which creates a possibility of exciton condensation along the lines first described by Keldysh and Kopaev.<sup>11</sup> The maximal possible symmetry of the order parameter is  $U(2)$ ; lattice effects bring it down to  $U(1)$ . The system in its low temperature phase is an insulator with a gapless collective mode, corresponding to fluctuations of spin density in the directions transverse to the applied magnetic field. The above is a brief summary of the discussion of Secs. II–IV. Section IV also contains a detailed phase diagram. The discussion in these sections dealt with the Landau-Ginzburg free energy functional written purely on symmetry grounds, where various energy scales of the system enter as parameters.

Section V contains a microscopic analysis tailored especially for graphene. The ultimate goal was to obtain estimates for the critical temperature and various parameters of the phase diagram, but a by-product of the analysis is a study

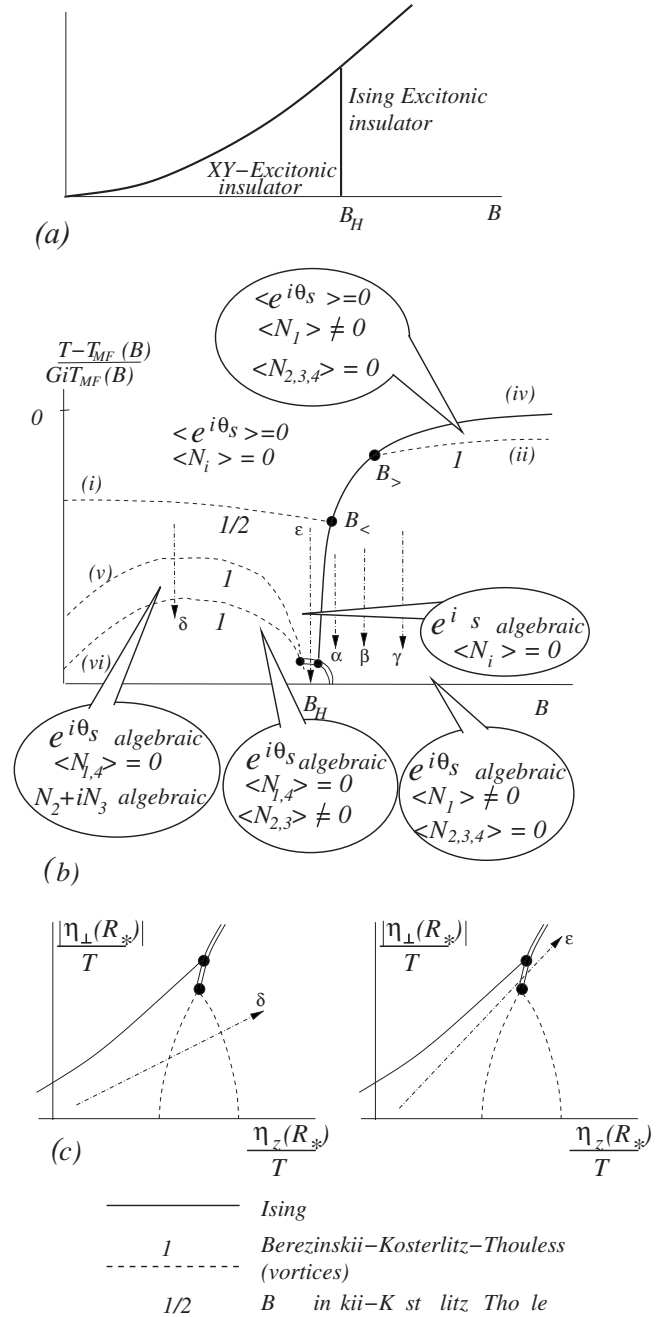


FIG. 19. Phase diagram of graphene in the parallel magnetic field for the short-range interaction constant  $F_-^z < 0$ . (a) Mean-field structure of the phase diagram. (b) The fine structure of the phase diagram in the close vicinity of the mean-field transition temperature,  $T_{MF}(B)$ . (c) Relation of the phase diagram (b) to the more general phenomenological phase diagram of Fig. 9. Cross sections denoted by  $\alpha$ ,  $\beta$ , and  $\gamma$  are shown in Fig. 18(c).

of how the strongest interaction in graphene—the Coulomb interaction—affects the spectrum and renormalizes other interactions (such as the short-range exchange). As is well known, the Coulomb interaction in graphene, measured by its dimensionless value  $g = \pi e^2 / 2v$ , is quite strong at energies of the order of the bandwidth. We have found, however, that the effective coupling steadily diminishes at low energies and asymptotically vanishes at  $E=0$ . The scale dependence

of  $g$  is rather slow and is given by Eq. (5.4). This formula includes an important scale  $\mathcal{R}$ , which we estimate for graphene as being of order  $10^2$ – $10^3$  lattice constants. This scale separates the region of relatively strong interaction, where  $g(r)$  decreases as a power law, from the region of weak coupling, where  $g(r) \sim [\ln r]^{-1}$ . It also sets the scale  $\mathcal{B}_0$  for the magnetic field (5.17) [our estimate is  $\mathcal{B}_0 \approx 10$ – $100$  K].

The renormalization process is drastically altered at energies of the order of the applied magnetic field  $\mathcal{B}$ . The field sets the ultraviolet cutoff for the physics of the excitonic insulator. However, the upper cutoff for its collective excitations is much lower, and is set by the value of the mean-field gap  $\Delta_0$ . One may anticipate that the latter energy scale is exponentially small in comparison with the cutoff  $\mathcal{B}$ . This is indeed the case, but, fortunately, the inverse coupling constant  $1/g(r \sim \mathcal{B}^{-1})$ , which stays in the exponent, depends rather weakly on the magnetic field [see Eqs. (5.29a) and (5.29b)] so that the magnitude of  $\Delta_0$  is not that small. Our estimate is that in fields of the order of or stronger than 10 T, the mean-field temperature is  $T_{MF} \leq 10^{-3} \mathcal{B}$ . This makes it possible to observe the excitonic effects described in this paper in the temperature range of tens of mK (see more discussion in Sec. V C).

Though the long-range Coulomb interaction is certainly the main player, its renormalization drags with itself weaker interactions, such as the short-range exchange, strengthening them at low energies. Such interactions break the U(2) symmetry present at low energies when only the long-range Coulomb interaction is taken into account. The analysis of Sec. V C 2 demonstrates that the U(2) symmetry survives in the excitonic insulator only at  $\mathcal{B} \leq \mathcal{B}_0$  when the estimated transition temperatures are probably too low for the effect to be observed. In the realistic region  $\mathcal{B} \geq \mathcal{B}_0$ , the anisotropy is strong. The expected phase diagrams in the  $\mathcal{B}$ - $T$  plane are given in Figs. 18 and 19 (they differ by a sign of a certain interaction parameter which, in the current stage, remains unknown]. Strong fields of the order of 10 T or more, which are required to make the excitonic insulator observable at temperatures above tens of mK, will probably put one in the regime marked by  $\beta$  or  $\gamma$  on the phase diagram of Figs. 18 and 19. The spin configuration corresponding to this regime is depicted in Fig. 3(d) and corresponds to the spin-flux phase.

#### ACKNOWLEDGMENTS

A.M.T. and D.E.K. were supported by the DOE under Contract No. DE-AC02-98 CH 10886. We acknowledge inspirational conversations with I. Zaliznyak, and interesting discussions with L. Levitov and M. Foster.

#### APPENDIX A: DERIVATION OF EQUATION (4.12)

Let us rewrite Eq. (4.4b) in a form

$$F_0 = \frac{\rho_K}{4} \text{Tr} \hat{j}_\mu^2 + \frac{\rho_S - \rho_K}{8} [\text{Tr} \hat{j}_\mu]^2, \quad (\text{A1})$$

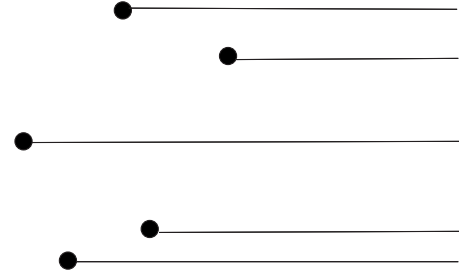


FIG. 20. Cuts on the  $x$ - $y$  plane attached to each topological defect in the five-vortex configuration.

where

$$\hat{j}_\mu \equiv -i \hat{V}^\dagger \partial_\mu \hat{V}. \quad (\text{A2})$$

The topological defects (4.8) and (4.10) are determined by the condition

$$\frac{1}{2\pi} \oint dx_\mu \text{Tr} \hat{j}_\mu = \pm 1; \pm \frac{1}{2}, \quad (\text{A3})$$

i.e.,

$$\theta = \frac{-i}{2} \text{Tr} \ln \hat{V} \quad (\text{A4})$$

must be a multivalued function of the coordinate.

In order to avoid the consideration of the multivalued field, we introduce cuts parallel to, say, the  $x$  axis, connecting each vortex or half-vortex with the boundary of the system (any physical quantity, obviously, does not depend on the choice of the cut) (see Fig. 20), and consider all the matrices to be single-valued functions but the phases experiencing the discontinuity on the cuts.

The current (A2) should be continuous, thus, we modify the definition as

$$\hat{j}_x = -i \hat{V}^\dagger \partial_x \hat{V},$$

$$\begin{aligned} \hat{j}_y = & -i \hat{V}^\dagger \partial_y \hat{V} + \pi \sum_{j=1}^{\mathcal{N}^{(1)}} l_j^{(1)} \delta(y - y_j^{(1)}) \text{sgn}(x - x_j^{(1)}) \\ & + \pi \sum_{j=1}^{\mathcal{N}^{(1/2)}} l_j^{(1/2)} \frac{1 + \mathbf{m}_j \cdot \boldsymbol{\sigma}}{2} \delta(y - y_j^{(1/2)}) \text{sgn}(x - x_j^{(1/2)}), \end{aligned} \quad (\text{A5})$$

where  $\mathcal{N}^{(1)}$  and  $\mathcal{N}^{(1/2)}$  are the number of the vortices and the vertices, respectively,  $x_j$  and  $y_j$  are their coordinates,  $l_j = \pm 1$  is the corresponding vorticity, and  $\mathbf{m}_j$  is the unit vector characterizing the spin of the  $j$ th half-vortex.

Writing the summation over the vortex and half-vortex coordinates explicitly, we obtain

$$\begin{aligned} \mathcal{Z} \propto & \sum_{\mathcal{N}^{(1)}=0}^{\infty} \frac{\mu_1^{\mathcal{N}^{(1)}\mathcal{N}^{(1)}}}{\mathcal{N}^{(1)}!} \prod_{j=1} \sum_{l_j^{(1)}=\pm 1} \int \frac{dx_j^{(1)} dy_j^{(1)}}{r_0^2} \sum_{\mathcal{N}^{(1/2)}=0}^{\infty} \frac{\mu_{1/2}^{\mathcal{N}^{(1/2)}\mathcal{N}^{(1/2)}}}{\mathcal{N}^{(1/2)}!} \prod_{j=1} \sum_{l_j^{(1/2)}=\pm 1} \int \frac{dx_j^{(1/2)} dy_j^{(1/2)} d\mathbf{m}_j}{4\pi r_0^2} \\ & \times \int \mathcal{D}\hat{V} \exp \left\{ - \int dx dy \left[ \frac{\rho_K}{4T} \text{Tr} \hat{j}_\mu^2 + \frac{\rho_s - \rho_K}{8T} (\text{Tr} \hat{j}_\mu)^2 \right] \right\}, \end{aligned} \quad (\text{A6})$$

where the matrix current  $\hat{j}_\mu$  is given by Eq. (A5).

After introducing the dual  $2 \times 2$  matrix field  $\hat{h} = \hat{h}^\dagger$ , Eq. (A6) acquires the form

$$\begin{aligned} \mathcal{Z} \propto & \sum_{\mathcal{N}^{(1)}=0}^{\infty} \frac{\mu_1^{\mathcal{N}^{(1)}\mathcal{N}^{(1)}}}{\mathcal{N}^{(1)}!} \prod_{j=1} \sum_{l_j^{(1)}=\pm 1} \int \frac{dx_j^{(1)} dy_j^{(1)}}{r_0^2} \sum_{\mathcal{N}^{(1/2)}=0}^{\infty} \frac{\mu_{1/2}^{\mathcal{N}^{(1/2)}\mathcal{N}^{(1/2)}}}{\mathcal{N}^{(1/2)}!} \prod_{j=1} \sum_{l_j^{(1/2)}=\pm 1} \int \frac{dx_j^{(1/2)} dy_j^{(1/2)} d\mathbf{m}_j}{4\pi r_0^2} \\ & \times \int \mathcal{D}\hat{V} \mathcal{D}\hat{h} \exp \left\{ - \int dx dy \left[ \frac{\rho_K}{4T} \text{Tr} \hat{j}_x^2 + \frac{T}{4\rho_K} \text{Tr} (\partial_x \hat{h})^2 + \frac{\rho_s - \rho_K}{8T} (\text{Tr} \hat{j}_x)^2 + \left( \frac{T}{8\rho_s} - \frac{T}{8\rho_K} \right) (\text{Tr} \partial_x \hat{h})^2 + i \text{Tr} \hat{j}_y \partial_x \hat{h} \right] \right\}, \end{aligned} \quad (\text{A7})$$

Substituting Eq. (A5) into Eq. (A7), integrating the terms with  $\delta$  functions by parts, and summing over  $l_j$ , we find

$$\begin{aligned} \mathcal{Z} \propto & \int \mathcal{D}\hat{V} \mathcal{D}\hat{h} \sum_{\mathcal{N}^{(1)}=0}^{\infty} \frac{\mu_1^{\mathcal{N}^{(1)}\mathcal{N}^{(1)}}}{\mathcal{N}^{(1)}!} \prod_{j=1} \int \frac{dx_j^{(1)} dy_j^{(1)}}{r_0^2} 2 \cos \pi \text{Tr} \hat{h}(r_j^{(1)}) \sum_{\mathcal{N}^{(1/2)}=0}^{\infty} \frac{\mu_{1/2}^{\mathcal{N}^{(1/2)}\mathcal{N}^{(1/2)}}}{\mathcal{N}^{(1/2)}!} \prod_{j=1} \\ & \times \int \frac{dx_j^{(1/2)} dy_j^{(1/2)} d\mathbf{m}_j}{4\pi r_0^2} 2 \cos \pi \left[ \text{Tr} \hat{h}(r_j^{(1/2)}) \frac{1 + \mathbf{m}_j \cdot \vec{\sigma}}{2} \right] \exp \left\{ - \int dx dy \left[ \frac{\rho_K}{4T} \text{Tr} \partial_x \hat{V}^\dagger \partial_x \hat{V} + \frac{T}{4\rho_K} \text{Tr} (\partial_x \hat{h})^2 \right. \right. \\ & \left. \left. + \frac{\rho_s - \rho_K}{8T} (-i \text{Tr} \hat{V}^\dagger \partial_x \hat{V})^2 + \left( \frac{T}{8\rho_s} - \frac{T}{8\rho_K} \right) (\text{Tr} \partial_x \hat{h})^2 + \text{Tr} \hat{V}^\dagger \partial_y \hat{V} \partial_x \hat{h} \right] \right\}. \end{aligned} \quad (\text{A8})$$

After the summation over  $\mathcal{N}^{(1/2)}$  and  $\mathcal{N}^{(1)}$ , and integration over  $\mathbf{m}_j$ , we obtain Eq. (4.12).

## APPENDIX B: ANALYSIS OF THE ISING PHASE TRANSITION

In the vicinity of  $T = \pi\rho_K$ , where the mutually dual cosines have the same scaling dimension 1, partition (4.26) can be mapped to the quantum many-body problem at zero temperature and then fermionized. The reader can consult Ref. 14, where the necessary information about the two-dimensional Ising model is provided. Choosing the  $y$  coordinate for imaginary time, we rewrite the classical Eq. (4.26)

$$\mathcal{Z} \propto \text{Tr} \exp \left( -L_y \int dx \hat{\mathcal{H}} \right),$$

$$\hat{\mathcal{H}} = \frac{\rho_K}{2T} (\partial_x \hat{\phi})^2 + \frac{T}{2\rho_K} (\partial_x \hat{\theta})^2 + \frac{\eta_\perp}{R^* T} \cos 2\hat{\phi} + \frac{\mu_{14}}{R^*} \cos(2\pi\hat{\theta}),$$

$$[\partial_x \hat{\phi}(x); \hat{\theta}(x')] = i\delta(x - x'). \quad (\text{B1})$$

Then using the fermionization rules

$$\hat{R}(x) \propto \exp[i\hat{\phi}(x) + i\pi\hat{\theta}],$$

$$\hat{L}(x) \propto \exp[-i\hat{\phi}(x) + i\pi\hat{\theta}], \quad (\text{B2})$$

we write down the corresponding one-dimensional quantum fermionic Hamiltonian density as

$$\begin{aligned} \hat{\mathcal{H}} = & i(L^+ \partial_x L - R^+ \partial_x R) + (\pi T / \rho_K - 1) R^+ R L^+ L + \eta_\perp (R^+ L \\ & + L^+ R) + \mu_{34} (R^+ L^+ + L R). \end{aligned} \quad (\text{B3})$$

It is convenient to decompose the Dirac spinor into the real (Majorana) components:

$$R = r_1 + ir_2, \quad L = l_1 + il_2, \quad (\text{B4})$$

where the corresponding operators are real ( $r_a = r_a^+, l_a = l_a^+$ ) and satisfy the following commutation relations:

$$\begin{aligned} \{r_a(x_1), r_b(x_2)\} &= \delta_{ab} \delta(x_{12}), \\ \{l_a(x_1), l_b(x_2)\} &= \delta_{ab} \delta(x_{12}), \quad \{r_a(x_1), l_b(x_2)\} = 0. \end{aligned} \quad (\text{B5})$$

Then Eq. (B3) becomes

$$\begin{aligned} \mathcal{H} = & \frac{i}{2} (l_a \partial_x l_a - r_a \partial_x r_a) + \tau (l_1 r_1) (l_2 r_2) + i(\eta_\perp / T + \mu_{34}) r_1 l_1 \\ & + i(\eta_\perp / T - \mu_{34}) r_2 l_2, \end{aligned} \quad (\text{B6})$$

where  $\tau = [T / (\pi\rho_K) - 1]$ . Hamiltonian (B6) describes two quantum Ising models coupled by the energy density operators. The original order parameter operator can be expressed in terms of order and disorder parameters of the Ising models  $\sigma$  and  $\mu$  (see Ref. 14 for the corresponding definitions):

$$e^{i\phi} = \sigma_1 \sigma_2 + i \mu_1 \mu_2. \quad (\text{B7})$$

The sign of the Majorana mass in the Ising model plays an important role, determining which operator ( $\sigma$  or  $\mu$ ) acquires a vacuum expectation value. Then from Eq. (B7), it is clear that this operator acquires a finite expectation value when the masses of the two species of Majorana fermions have the same sign, so that either  $\sigma_a$  or  $\mu_a$  fields condense simultaneously. The high temperature phase is characterized by masses of different signs.

At small  $|\tau| \ll 1$ , we can use perturbation theory to write the equations for the masses (let us choose  $\eta_\perp > 0$ ):

$$m_1 = (\eta_\perp/T + \mu_{34}) > 0,$$

$$m_2 = \left( \frac{\eta_\perp}{T} - \mu_{34} \right) + \frac{\tau}{2\pi} m_1 \ln \left( \frac{1}{R^* |m_1|} \right). \quad (\text{B8})$$

It follows that  $m_2$  changes sign at

$$\frac{T_c}{\pi \rho_K} - 1 = \frac{\eta_\perp/T - \mu_{34}}{\eta_\perp/T + \mu_{34}} \ln \left( \frac{1}{R^* (\eta_\perp + \mu_{34})} \right), \quad (\text{B9})$$

where the second order phase transition from disordered (high temperature) to ordered (low temperature) state takes place. Equation (B9) agrees with Eq. (4.30).

- 
- <sup>1</sup>K. S. Novoselov, A. K. Geim, S. V. Morozov, D. Jiang, Y. Zhang, S. V. Dubonos, I. V. Grigorieva, and A. A. Firsov, *Science* **306**, 666 (2004).
- <sup>2</sup>For a recent progress review, see A. K. Geim and K. S. Novoselov, *Nat. Mater.* **6**, 183 (2007).
- <sup>3</sup>K. S. Novoselov, A. K. Geim, S. V. Morozov, D. Jiang, M. I. Katsnelson, I. V. Grigorieva, S. V. Dubonos, and A. A. Firsov, *Nature (London)* **438**, 197 (2005).
- <sup>4</sup>Y. Zhang, Y. W. Tan, H. L. Stormer, and P. Kim, *Nature (London)* **438**, 201 (2005).
- <sup>5</sup>D. V. Khveshchenko, *Phys. Rev. Lett.* **87**, 246802 (2001); D. V. Khveshchenko and H. Leal, *Nucl. Phys. B* **687**, 323 (2004); D. V. Khveshchenko and W. F. Shively, *Phys. Rev. B* **73**, 115104 (2006).
- <sup>6</sup>A. A. Abrikosov and S. D. Beneslavskii, *Sov. Phys. JETP* **32**, 699 (1971).
- <sup>7</sup>J. Gonzalez, F. Guinea, and M. A. H. Vozmediano, *Phys. Rev. B* **59**, R2474 (1999).
- <sup>8</sup>D. T. Son, *Phys. Rev. B* **75**, 235423 (2007).
- <sup>9</sup>For a general construction of the terms compatible with the lattice symmetries, see G. L. Bir and G. E. Pikus, *Symmetry and Strain-Induced Effects in Semiconductors* (Wiley, New York, 1974).
- <sup>10</sup>We use parametrization as in I. L. Aleiner and K. B. Efetov, *Phys. Rev. Lett.* **97**, 236801 (2006).
- <sup>11</sup>L. V. Keldysh and Y. V. Kopayev, *Sov. Phys. Solid State* **6**, 2219 (1965).
- <sup>12</sup>V. L. Berezinskii, *Sov. Phys. JETP* **32**, 493 (1971).
- <sup>13</sup>J. M. Kosterlitz and D. J. Thouless, *J. Phys. C* **5**, L124 (1972); **6**, 1181 (1973).
- <sup>14</sup>A. M. Tselik, *Quantum Field Theory in Condensed Matter Physics*, 2nd ed. (Cambridge University Press, Cambridge, England, 2003).
- <sup>15</sup>In the mean-field picture, the existence of such lines and the points where three continuous phase transitions intersect is not possible [see Sec. 150 of L. D. Landau and E. M. Lifshits, *Statistical Physics* (Pergamon, New York, 1986)], and the critical line  $B_1 - B'_1$  [see Fig. 5(a)] becomes either the first order phase transition line or splits into two second order phase transition lines. The existence of this line is a consequence of the fluctuations, making the vortex operator  $\cos 2\pi h_s$  vanish.
- <sup>16</sup>A. A. Abrikosov, L. P. Gorkov, and I. E. Dzyaloshinskii, *Methods of Quantum Field Theory in Statistical Physics* (Prentice-Hall, New York, 1963).
- <sup>17</sup>See, e.g., Z. Jiang, E. A. Henriksen, L. C. Tung, Y.-J. Wang, M. E. Schwartz, M. Y. Han, P. Kim, and H. L. Stormer, *Phys. Rev. Lett.* **98**, 197403 (2007); R. S. Deacon, K.-C. Chuang, R. J. Nicholas, K. S. Novoselov, and A. K. Geim, *Phys. Rev. B* **76**, 081406(R) (2007).
- <sup>18</sup>Formula (5.9) for  $r_c \gg \mathcal{R}$  was first obtained by I. L. Aleiner and V. I. Falko (unpublished).
- <sup>19</sup>D. A. Abanin, P. A. Lee, and L. S. Levitov, *Phys. Rev. Lett.* **98**, 156801 (2007).
- <sup>20</sup>I. F. Herbut, *Phys. Rev. B* **75**, 165411 (2007).
- <sup>21</sup>E. McCann, K. Kechedzhi, V. I. Fal'ko, H. Suzuura, T. Ando, and B. L. Altshuler, *Phys. Rev. Lett.* **97**, 146805 (2006).
- <sup>22</sup>Detailed calculation of the polarization operator at finite doping can be found in B. Wunsch, T. Stauber, F. Sols, and F. Guinea, *New J. Phys.* **8**, 318 (2006). For our purposes, it is important only that  $\Pi(0, q)$  does not depend on the wave vector at all for  $q < 2k_F$ .
- <sup>23</sup>This idea belongs to I. Zaliznyak (private communication).